Modeling magnetosensitive ion channels in the viscoelastic environment of living cells

Igor Goychuk*

Institute for Physics and Astronomy, University of Potsdam, Karl-Liebknecht-Strasse 24/25, 14476 Potsdam-Golm, Germany

(Received 29 July 2015; published 23 October 2015)

We propose and study a model of hypothetical magnetosensitive ionic channels which are long thought to be a possible candidate to explain the influence of weak magnetic fields on living organisms ranging from magnetotactic bacteria to fishes, birds, rats, bats, and other mammals including humans. The core of the model is provided by a short chain of magnetosomes serving as a sensor, which is coupled by elastic linkers to the gating elements of ion channels forming a small cluster in the cell membrane. The magnetic sensor is fixed by one end on cytoskeleton elements attached to the membrane and is exposed to viscoelastic cytosol. Its free end can reorient stochastically and subdiffusively in viscoelastic cytosol responding to external magnetic field changes and can open the gates of coupled ion channels. The sensor dynamics is generally bistable due to bistability of the gates which can be in two states with probabilities which depend on the sensor orientation. For realistic parameters, it is shown that this model channel can operate in the magnetic field of Earth for a small number (five to seven) of single-domain magnetosomes constituting the sensor rod, each of which has a typical size found in magnetotactic bacteria and other organisms or even just one sufficiently large nanoparticle of a characteristic size also found in nature. It is shown that, due to the viscoelasticity of the medium, the bistable gating dynamics generally exhibits power law and stretched exponential distributions of the residence times of the channels in their open and closed states. This provides a generic physical mechanism for the explanation of the origin of such anomalous kinetics for other ionic channels whose sensors move in a viscoelastic environment provided by either cytosol or biological membrane, in a quite general context, beyond the fascinating hypothesis of magnetosensitive ionic channels we explore.

DOI: 10.1103/PhysRevE.92.042711 PACS number(s): 87.50.C−, 05.40.−a, 05.10.Gg, 87.10.Mn

I. INTRODUCTION

Evidence of the influence of weak electromagnetic fields including magnetic fields on many living organisms abounds [1–9]. Most spectacular and doubtless of such manifestations are related to the navigation of honeybees, fishes, birds, rats, bats, and other animals [4,10–13] in the magnetic field of Earth of about $B_e = 50\ \mu T$ in strength. Various hypotheses related to profoundly different physical mechanisms have been suggested to explain this influence. They range from nonthermal quantum mechanisms related to spin-dependent electron transfer [4,14], which circumvent the so-called "kT" problem [5,8,15], to a variety of classical mechanisms based on a widespread occurrence of biomagnetite nanoparticles in tissues of many living organisms starting from magnetotactic bacteria [16–19] and ending at the human brain [20]. Magnetite (Fe_3O_4) has a saturation magnetization of $M_s = 4.8 \times 10^5$ A/m, and elongated magnetite nanoparticles are in a single domain ferrimagnetic state when their sizes range from 20 to 200 nm depending on the short-to-long axis aspect ratio (shape factor) [11]. Hence, the magnetic energy of a spherical magnetosome (magnetic nanoparticle dressed in a lipid-protein membrane shell [17]) of radius 100 nm and magnetic dipole moment $\mu \approx 2$ fA m^2 is as large as $E_B = \mu B_e \sim 24.5\ k_B T$ when its magnetic moment is aligned with Earth's magnetic field. The whole cells with magnetic moments in the range $\mu \sim 4$–100 fA m^2 were identified recently as candidate magnetoreceptor cells in trout olfactory epithelium [21]. Another recent study [22] confirms the existence of cells possessing such large magnetic moments in both trout and pigeons. However, it expresses doubt that this magnetic moment is caused by biomagnetite and not by magnetic nanoparticles polluting the environment, which are absorbed to the cell membranes. In this respect, the presence of iron-rich organelles filled by ferrihydrate in the hair cells of pigeons [22] can give support to a biological origin of magnetite therein, rather than the contrary. Even though the biochemical pathway of biomagnetite synthesis remains still controversial [17], the presence of ferrihydrate indirectly supports one of biochemical schemes suggested earlier [10]. Furthermore, about 10% of biomagnetite particles found in human brain [12,20] (about 10^6 or even 10^8 per one gram of tissue in gray matter and in meninges, correspondingly, and about 50 ng/g in hippocampus on average [23]) are about 100 nm or larger in size. In bacteria, the length of elongated magnetoparticles can reach 110 nm with shape factor 0.8–0.9 [18] and even larger, up to 200 nm [19]. It is important that genes encoding magnetosome specific proteins in some bacteria were identified [17]. This provides one of the strongest arguments in favor of a biological origin of magnetite in biological cells.

Importantly, the magnitude of a magnetic field produced by a spherical magnetosome can reach (at peak of a highly anisotropic distribution) $B_{\rm mag} \sim 402$ mT near its surface (see Appendix A), independently of its radius. This is about 8000 times larger than B_e. Thus, quantum magnetic effects can also be mediated by the magnetic near field of a magnetosome reorienting in an external magnetic field and positioned near an electron-transferring magnetosensitive molecular complex, rather than directly by an external field itself [24]. The particles of intermediate size $55 \times 44 \times 44$ nm, typical for magnetosomes found in magnetotactic bacteria [25], have $E_B \sim 0.623\ k_B T$, and they easily make chains joined by magnetic cohesion force, being rigid enough [26] in not too

*igoychuk@uni-potsdam.de

strong magnetic fields, smaller than 30 mT [27]. Hence, a rod consisting of five such nanoparticles with magnetic moments aligned has $E_B \sim 3.12\, k_BT$, and it can easily serve as quite a classical, compasslike sensor element for magnetosensitive ion channels, as shown in this paper. When an external field becomes compatible with $B_{\rm mag}$ it can disrupt the magnetosome chain or make it unstable [27]. This is why such a sensor will not work in too strong fields. It will be literally broken in pieces, presenting a disordered cluster of nanoparticles. For another typical size, $103 \times 85 \times 85$ nm, also commonly found in bacteria [18], $E_B \sim 4.23\, k_BT$ for a single magnetosome. Hence, a sensor can consist also of a single nanoparticle.

The idea that a magnetic nanorod can serve as a sensor and transducer of magnetic field torque was first suggested by Yorke [28]. Kirschvink [11,12] proposed that it can be a magnetosensitive ion channel involved with a spherical magnetosome attached to a cytoskeleton element near an ion channel in biological membrane and coupled by an elastic linker to the ion channel gating machinery. An external magnetic field creates a torque on the magnetosome, which rotates and opens the ion channel. The sensor is considered to be essentially monostable in the Kirschvink model. This model has been refined recently for the chain of magnetosomes serving as sensor [29], but remained monostable as in the original proposal. Binhi and Chernavsky proposed a different model [24], based on the bistability of magnetosome rotations induced by a magnetic field for a spherical magnetosome elastically coupled to cytoskeleton. It is not related to gating of ionic channels. Rather a change in distribution of the magnetic field induced by magnetosome is of interest in the context of a related quantum mechanism [24,30]. Furthermore, it has been shown recently that streptavidin-linked magnetite nanoparticles of 50 nm size (in radius on average) can induce ion channel like activity being absorbed on phospholipid bilayer [31]. The corresponding ion current recordings resemble somewhat the ion channel activity induced in electric fields by alamethicin peptides inserted into the membrane [32].

In this paper a further generalization of the model by Kirschvink *et al.* is suggested and studied. The generalization consists of several profound aspects. First, the stochastic motion of the sensor is considered to be bistable because of bistability of the ion channel gate to which the sensor is coupled. Such a bistability is a common point in describing stochastic dynamics of ionic channels [33]. To include it in the sensor dynamics, we adopt a gating spring model [34] assuming that the gate can take on just two conformations, open and closed. A similar model has originally been suggested in relation to the hair cell dynamics. Second, we consider a possibility that a magnetic sensor can be coupled to gates of several ionic channels making a cluster, i.e., that a compact cluster of ionic channels and a magnetic nanoparticle serving as sensor make a magnetosensitive complex in a biological membrane. This can explain why such magnetosensitive ion channels, as separate units, were not found thus far. Third, and most important in a more general context of gating stochastic dynamics of ionic channels, we consider the influence of the viscoelasticity of the environment in which the sensor is moving on the sensor dynamics. We show that viscoelasticity alone can result in profoundly nonexponential residence time distributions of the channels in their open and closed states, such as stretched exponential distribution [35,36] and power law distributions [35,37–41]. This explanation of unusual gating kinetics is different from other physical theories suggested thus far, which are based, in particular, on a complex free energy landscape for sensor or conformational dynamics of the whole ion channel with very many multiply degenerated minima and maxima (glasslike dynamics) [42–44]. The latter one can be modeled in the simplest possible fashion as a continuous normal diffusion in a potential box, which already makes it possible to explain [45] the origin of the $-3/2$ power law in the distribution of closed times [38,39] in conjunction with the origin of Hodgkin-Huxley voltage dependence [33,45]. Such normal diffusion can become also anomalously slow (fractional diffusion), a modeling pathway explored in [46].

Recent work [47,48] suggests, however, that the discussed anomalous kinetics can also result from the standard bistable dynamics of a sensor, commonly assumed in biophysics textbooks [33], as a manifestation of memory effects caused by the viscoelasticity of the environment. This is a very appealing and simple physical explanation indeed. In this respect, both cytosol and the plasma membrane are viscoelastic [48,49]. Hence, viscoelasticity is considered to be a major cause of experimentally observed anomalous diffusion in crowded colloidal and polymer solutions [50–56] and living cells [57–60], as well as in single protein molecules [61]. To study such effects, the approach of the generalized Langevin equation (GLE) characterized by a power law scaling memory kernel and power law correlated thermal noise of environment, which are related by fluctuation-dissipation theorem (FDT), provides a major well-established theoretical framework in the case of linear dynamics [50,54]. It is not easy to generalize this framework towards nonlinear dynamics in bi- and multistable potentials. For example, a corresponding *exact* Fokker-Planck description which would mirror and complement the GLE approach, like in the case of memoryless dynamics, has simply not been developed thus far for potentials other than linear and parabolic [62]. In other words, any nonlinearity creates a problem for Fokker-Planck description of such a dynamics with memory [47,48,63]. Recently, we bypassed such difficulties within the GLE approach using the road of multidimensional Markovian embedding of GLE dynamics within a generalized Maxwell-Langevin model of viscoelasticity [47,48]. It has also been generalized to include negative correlations of stochastic force and corresponding memory effects leading to superdiffusion and supertransport [64]. The utility of this approach has been demonstrated on various basic models of nonlinear stochastic dynamics such as bistable dynamics [47], washboard dynamics [47,48,65], anomalous rocking ratchets [48,66–69], and anomalous flashing ratchets [70], as well as applications to molecular motor dynamics in viscoelastic cytosol [71–73].

In the context of magnetosomes dynamics in viscoelastic cytosol, Kirschvink *et al.* have repeatedly taken the cytosol influence into account by enhancing the coefficient of *normal* viscous friction experienced by magnetosome by a factor of about 100 [12,21]. This was a standard way to think about the influence of viscoelasticity and crowding in cytosol in biological applications until recently [74]. However, recent results on anomalous diffusion of nano- and submicron

particles in living cells suggest that this enhancement can be much larger, of the order of 1000, and even larger [57,71,75], depending, in particular, on the size of particle [76]. Cytosol seem to operate normally at the edge of a phase transition from a liquidlike state to a solidlike state with broken ergodicity [77]. Moreover, even for the enhancement factor 100, the bistable orientational dynamics of magnetic nanoparticles would be so slow, as we show in this paper, that it would be completely out of interest within a biological context. However, a major effect, which introduces viscoelasticity, is the emergence of transient subdiffusion which is much faster than the asymptotic limit of normal diffusion. In fact, this asymptotic regime can become completely irrelevant for mesoscopic dynamics. This paradoxical fact also follows from the non-Markovian rate theory developed beyond the standard memoryless Kramers theory [78–82]; see [83] for a review and below. Namely, this "much faster, not slower" [75,84,85], paradoxically due to subdiffusion, makes operating such bistable magnetic sensors possible in viscoelastic cytosol. This provides one of the most important results of this work, which lends further support to the idea of magnetic field sensing with classical dynamics of sufficiently large biomagnetite nanoparticles.

II. MODEL AND THEORY

We consider the following model. A biomagnetite rod made of a chain of magnetosomes of total length L or a single elongated magnetic nanoparticle can rotate with one end fixed, e.g., on on a cytoskeleton meshwork attached to the cell membrane inside the cell (see Fig. 1 for an idea). It is also elastically attached to the gates of ionic channels (one is shown) by flexible linkers, which are modeled here within a finite extensible nonlinear elastic (FENE) model [86]. The channel gate, or rather a molecular latch, which fixes the gate in its either open or closed state, can be in two states. The closed state is characterized by the energy ϵ_1, and the open one has the energy $\epsilon_2 - f_0 x$, which depends on the linker elongation x, where f_0 is a force constant characterizing the strength of coupling (force exerted by the linker on the gate). Elastic energy is $U_{\rm FENE}(x) = -\frac{1}{2}kl_{\rm max}^2 \ln(1 - x^2/l_{\rm max}^2)$ within the FENE model, where k is elastic spring constant and $l_{\rm max}$ is the maximal extension length of the linker when it is fully stretched. The statistical mean force exerted by the channel gate on the linker can be found as $f(x) = -dG(x)/dx$ from the potential of the mean force $G(x) = -k_BT \ln Z(x)$, where $Z(x) = \exp[-\beta\epsilon_1] + \exp[-\beta(\epsilon_2 - f_0 x)]$ is the statistical sum of the gate and $\beta = 1/(k_BT)$ is the inverse temperature. Here one implicitly assumes that the gate-latch dynamics (transitions between two states) is very fast and, hence, the actual gating dynamics is enslaved by the sensor dynamics and reflects the latter one. Mean force is $f(x) = f_0 p(x)$, where

$$p(x) = \frac{1}{1 + \exp[-f_0(x - l_0)/(k_BT)]} \tag{1}$$

is that probability of the gate being open and $l_0 = (\epsilon_2 - \epsilon_1)/f_0$. In order to define some x_0 as the equilibrium point, we follow [34] and redefine mean force by a shift as $f(x) = f_0[p(x) - p(x_0)]$. The motion of the rod is assumed to be restricted to the plane orthogonal to the membrane and characterized by the angle ϕ, $0 \leqslant \phi \leqslant \pi$, counted from the membrane plane in the counterclockwise direction. The linker elongation is approximated as $x(\phi) = 2l[\sin(\phi/2) - \sin(\phi_0/2)]$, where l is the rotation arm, and ϕ_0 is an equilibrium angle. The external magnetic field B is directed at the angle ψ within the plane of motion. The potential of mean force (torque) acting on the rod in our model is

$$\begin{aligned} U(\phi) = &-\tfrac{1}{2}kl_{\rm max}^2 \ln\{1 - [x(\phi)/l_{\rm max}]^2\} \\ &- k_BTm \ln\{1 + \exp[f_0(x(\phi) - l_0)/(k_BT)]\} \\ &+ mf_0 p(\phi_0)x(\phi) - \mu B\cos(\psi - \phi), \end{aligned} \tag{2}$$

where $p(\phi_0) = p[x = 2l\sin(\phi_0/2)]$, μ is the magnetic moment of the rod, and m is the number of ion channels coupled to the sensor and treated in a mean-field fashion (all gates move synchronously enslaved by the same sensor). We scale the energy in units of $U_0 = kl^2$, temperature in units of U_0/k_B, distances in units of l, and forces in units of $f_u = U_0/l$. U_0 will be fixed to $U_0 = 10\ k_BT_r \approx 41$ pN nm ≈ 0.25 eV, where T_r is a typical room temperature, $T_r \approx 297$ K. For a typical $k = 0.3$ pN/nm [87], this corresponds to $l \approx 11.69$ nm and force units $f_u \approx 3.51$ pN. For the purpose of illustration, the magnetic nanorod is assumed to be made of magnetosomes of size $55 \times 44 \times 44$ nm^3. For the magnetosome core made of magnetite with saturating magnetization of $M_s = 480$ kA/m, its elementary magnetic moment is $\mu_1 \approx 0.0511$ fA m^2 and its energy in the magnetic field of Earth taken to be $B = B_e = 50\ \mu$T is $\mu_1 B \approx 0.623\ k_BT_r$, when it is aligned with the field direction. The sensor can be operable already for $n = 5$ nanoparticles in the rod with $\mu_5 B = 5\mu_1 B \approx 3.115\ k_BT_r$, and a reliable operation can be achieved for $n = 7$ with $\mu_7 B = 7\mu_1 B \approx 4.363\ k_BT_r$. For these two values we do illustrative calculations below, noting once again, however, that the sensor can consist also of just one sufficiently large ferro- or ferrimagnetic nanoparticle. For example, a particle with the size $103 \times 85 \times 85$ nm^3 will have about the same $\mu B \approx 4.36\ k_BT_r$ as our rod with $n = 7$, and such nanoparticles are also customarily found in living species. Some examples of $U(\phi)$ for various magnetic energies and the corresponding $p(\phi)$ are plotted in Fig. 2.

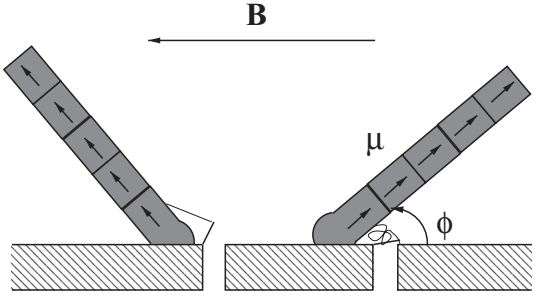

FIG. 1. Illustration of the considered model of the magnetosensitive ion channel expressing the idea. Proportions are not held. The rotation of the nanorod is coupled via flexible linkers to gates of ion channels, which can form a cluster. One channel is shown for simplicity.

Consider first the $B = 0$ case (solid line) and notice that when $U(\phi)$ arrives at its maximum at $\phi_{\rm max} \approx 103.3^\circ$, $p(\phi_{\rm max}) \approx 0.269$. For $\phi \geqslant \phi_{\rm max}$, a further increase of ϕ

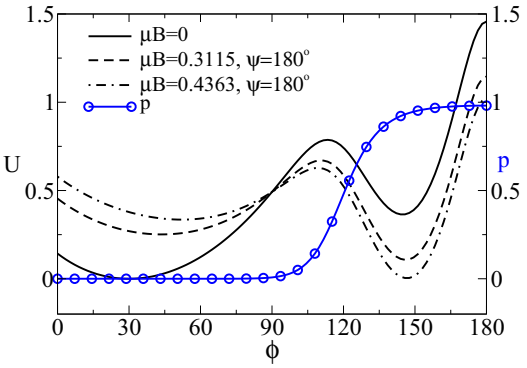

FIG. 2. (Color online) Orientational potential $U(\phi)$ and opening probability $p(\phi)$ (blue line with circles) of the ion channel versus angle ϕ in degrees. Potential box walls are imposed for $\phi < 0$ and $\phi > \pi$ restricting motion to one side of membrane. A magnetic field is applied at an angle $\psi = 180^\circ$, and $\phi_0 = 30^\circ$. Model parameters: $T = 0.1$, $l_{\max} = 1.5$, $f_0 = 1.5$, $l_0 = 1.22$, and $m = 7$ channels in the sensor cluster. The gating energy difference $\epsilon_2 - \epsilon_1 = f_0 l_0 = 1.83$, or 18.3 in units of $k_B T_r$.

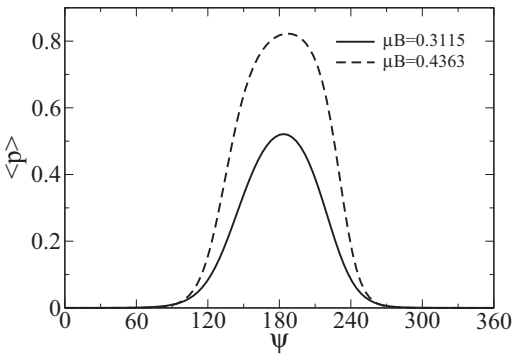

FIG. 3. Averaged probability of the channels to be open as a function of magnetic field orientation for two values of μB shown in the plot. Model parameters: $\phi_0 = 30^\circ$, $T = 0.1$, $l_{\max} = 1.5$, $f_0 = 1.5$, $l_0 = 1.22$, and $m = 7$ channels in the sensor cluster.

introduces a negative stiffness instability and the rod rotates to a new metastable minimum at $\phi_{\min,2} \approx 144.81^\circ$, where the channel opening probability becomes $p(\phi_{\min,2}) \approx 0.926$. At the first metastable minimum, $\phi_{\min,1} = \phi_0 = 30^\circ$, $p(\phi_{\min,1}) \approx 10^{-8}$. The corresponding energy difference between two metastable minima is $\Delta U = U(\phi_{\min,2}) - U(\phi_{\min,1}) \approx 0.3639 = 3.639\, k_B T_r$, and the energy barriers are $\Delta U_1 = U(\phi_{\max}) - U(\phi_{\min,1}) \approx 0.787 = 7.87\, k_B T_r$, and $\Delta U_2 = U(\phi_{\max}) - U(\phi_{\min,2}) \approx 0.4232 = 4.232\, k_B T_r$. Being attached to a common sensor, the channels fluctuate stochastically but synchronously between their closed and open states following the sensor motion, with the averaged opening probability, which can be roughly estimated as $\langle p \rangle \sim 1/\{1 + \exp[\Delta U/(k_B T_r)]\} \approx 0.026$ (at room temperatures); i.e., the channels are closed most of time. Actually, the opening probability will be lower than this rough estimate because the first minimum is shallower than the second one; i.e., it is also entropically preferred. Judging from the value of ΔU, one can expect that, for a sufficiently strong magnetic field at a proper angle ψ such that $\mu B \sim \Delta U$, the second metastable minimum can be made lower relative the first one and the channel will become open on average. Indeed, this is the case already for $\mu B = 0.3115 U_0 = 3.115\, k_B T_r$ at $\psi = \pi$; see Fig. 2. The entropic effects may, however, compensate somewhat for the field-induced negative ΔU, and the channels are indeed about half-open on average; see below. For a larger $\mu B = 0.4363 U_0 = 4.363\, k_B T_r$ in Fig. 2, the channels will predominantly be open.

A. Averaged open probability and ionic current as functions of field direction

The averaged probability of the channel to be open can be found as

$$\langle p(B,\psi) \rangle = \int_0^\pi p(\phi) e^{-U(\phi)/(k_B T)} d\phi / Z, \qquad (3)$$

where $Z = \int_0^\pi e^{-U(\phi)/(k_B T)} d\phi$ is the corresponding statistical sum (integral). It accounts also for entropic effects. Unfortunately, this expression cannot be found in a closed compact analytic form for the model considered. However, its numerical evaluation can be easily done. The corresponding results are shown in Fig. 3 and reveal that the direction of magnetic field can be detected by a bell-shaped increase of the opening probability within the angle $\Delta\psi \sim 180^\circ \pm 60^\circ$. Further sharpening of the detection of the field direction can be achieved via an adjusted threshold of excitation in the sensory cell.

The averaged ionic current conducted by this sensory complex is thus $\langle I \rangle = m i_0 \langle p(B,\psi) \rangle$, where i_0 is the unitary current through one open channel. Let us estimate it with $i_0 = 50$ pA being a typical value for large conductance cation channels [33]. These should be either sodium or calcium channels in order to cause depolarization of the cell membrane by their opening, given typically small out-of-equilibrium inner-cell concentrations of sodium and calcium ions with respect to the cell exterior. Then, for $m = 7$ and $\langle p \rangle = 0.5$, $\langle I \rangle = 175$ pA. Estimating the whole cell membrane resistance at rest as $R = 100$ MΩ [88], the transmembrane potential change is estimated as $\Delta V = R\langle I \rangle \sim 17.5$ mV. This can already be sufficient to depolarize an excitable cell membrane and to trigger a spiking activity mediating further information about external magnetic field changes. However, a detailed elaboration of related excitable cell model in the spirit of the Hodgkin-Huxley type conductances based approach is beyond the scope of the present work and is left for the future.

B. Stochastic dynamics

In order to operate as a sensor, the opening-closing stochastic dynamics of the considered magnetic sensor should also be sufficiently fast. Clearly, if it would take minutes, on average, to accomplish transitions to the open state, such a sensor would simply be too slow to be of any relevance in biology. The motion of the sensor occurs in viscoelastic cytosol. It is considered to be overdamped with the inertial effects neglected. Apart from the mean torque $f(\phi) = -dU(\phi)/d\phi$, it is subjected to viscoelastic memory-friction torque $-\int_0^t \eta_{\rm mem}(t-t')\dot{\phi}(t')dt'$, which acts in addition to the viscous Stokes friction torque, $-\eta_0\dot{\phi}$, caused by the

primary water component of cytosol. The dissipative forces are complemented by the corresponding zero-mean Gaussian thermal random noises of the environment at temperature T, $\xi_{\rm mem}(t)$ and $\xi_0(t)$, correspondingly. The friction and thermal noise are related by the (second) FDT by Kubo [89–91],

$$\langle \xi_{\rm mem}(t)\xi_{\rm mem}(t')\rangle = k_B T \eta_{\rm mem}(|t-t'|), \tag{4}$$

$$\langle \xi_0(t)\xi_0(t')\rangle = 2k_B T \eta_0 \delta(t-t') \, . \tag{5}$$

This ensures thermal detailed balance in the absence of external driving. Stochastic dynamics is described by the GLE [89–92],

$$\eta_0 \dot{\phi} = f(\phi) - \int_0^t \eta_{\rm mem}(t-t')\dot{\phi}(t')dt' + \xi_{\rm mem}(t) + \xi_0(t). \tag{6}$$

The memory kernel reflecting the viscoelasticity of complex polymeric fluids such as cytosol has often an intermediate power law scaling $\eta_{\rm mem}(t) = \eta_\alpha t^{-\alpha}/\Gamma(1-\alpha)$ between two memory cutoffs, τ_l and τ_h, with $0 < \alpha < 1$. It corresponds to a complex shear modulus $G^*(\omega) \propto \omega^\alpha$ [50,54] at intermediate frequencies in accordance with a huge body of rheology [93,94] and microrheology research [51–54,56,57]. η_α is a fractional friction coefficient [48,95] corresponding to a fractional viscosity coefficient ζ_α [93], $\eta_\alpha \propto \zeta_\alpha$. A strict power law is clearly an idealization and cutoffs must be present on physical grounds. The short time cutoff τ_l reflects the molecular size effects or highest vibrational modes present in the environment (which cannot be captured by any continuous medium type approximation). The long time cutoff τ_h must also be present in any fluidlike environment making the overall integral $\eta_{\rm eff} = \int_0^\infty \eta_{\rm mem}(t)dt$ finite. This reflects a finite macroscopic viscosity $\zeta_{\rm eff} \sim \eta_{\rm eff}$ of such complex fluids on a large time scale $t \gg \tau_h$. The model with $\tau_l \to 0$, $\tau_h \to \infty$ (strict power law scaling) corresponds to the so-called fractional Langevin equation (FLE) upon using the formalism of fractional time derivatives [63,69,92,96,97] or a strict sub-Ohmic memory friction within dynamical approach to generalized Brownian motion [90,98]. Then the solution of a potential-free FLE (6), $f(\phi) = 0$, with the Stokes friction neglected, $\eta_0 \to 0$, and for ϕ regarded as a linear, rather than cyclic variable, is fractional Brownian motion (fBm) [48,63]. It presents a Gaussian process with stationary increments and a long-range memory, which is completely characterized by its variance, $\langle \delta\phi^2\rangle = 2D_\alpha t^\alpha/\Gamma(1+\alpha)$, growing sublinearly. The fractional (orientational) diffusion coefficient D_α is related to the fractional friction coefficient η_α by the generalized Einstein relation, $D_\alpha = k_B T/\eta_\alpha$. Upon taking the Stokes friction into account it becomes [69],

$$\langle \delta\phi^2(t)\rangle = 2D_0 t E_{1-\alpha,2}[-(t/\tau_{\rm in})^{1-\alpha}], \tag{7}$$

where $E_{a,b}(z) := \sum_0^\infty z^n/\Gamma(an+b)$ is generalized Mittag-Leffler function, and $D_0 = k_B T/\eta_0$ is a normal diffusion coefficient. Furthermore, $\tau_{\rm in} = (\eta_0/\eta_\alpha)^{1/(1-\alpha)}$ is a transient time constant. For $t \ll \tau_{\rm in}$, diffusion is initially normal, $\langle \delta\phi^2(t)\rangle \approx 2D_0 t$. It becomes anomalously slow, $\langle (\delta\phi)^2\rangle = 2D_\alpha t^\alpha/\Gamma(1+\alpha)$, for $t \gg \tau_{\rm in}$. We take further advantage of the approximation of the power-law scaling memory kernel by a sum of the exponentials [47,48],

$$\eta_{\rm mem}(t) = \sum_{i=1}^N k_i \exp(-\nu_i t), \tag{8}$$

with a fractal scaling of relaxation rates $\nu_i = \nu_0/b^{i-1}$ and weights $k_i \propto \nu_i^\alpha$ (having physical dimension of energy in the present case) to embed non-Markovian dynamics of $\phi(t)$ as a component or projection of $N+1$-dimensional Markovian dynamics,

$$\begin{aligned} \eta_0\dot{\phi} &= f(\phi) - \sum_{i=1}^N k_i(\phi - y_i) + \xi_0(t), \\ \eta_i \dot{y}_i &= k_i(\phi - y_i) + \xi_i(t), \end{aligned} \tag{9}$$

where y_i are nondimensional linear auxiliary variables, $\eta_i = k_i/\nu_i$, and $\xi_i(t)$ are independent auxiliary white Gaussian noises obeying

$$\langle \xi_i(t)\xi_j(t')\rangle = 2\delta_{ij}k_B T \eta_j \delta(t-t') \tag{10}$$

and also independent of $\xi_0(t)$. The initial positions $y_i(0)$ are sampled from a Gaussian distribution centered around $\phi(0)$, $\langle y_i(0)\rangle = \phi(0)$ with variances $\langle [y_i(0) - \phi(0)]^2\rangle = k_B T/k_i$, in order to have complete equivalence with the corresponding GLE in Eqs. (4)–(6) and (8) in the ensemble sense [48]. It is convenient to choose

$$k_i = \nu_0 \eta_{\rm eff} \frac{b^{1-\alpha} - 1}{b^{(i-1)\alpha}[b^{N(1-\alpha)} - 1]}, \tag{11}$$

where $\nu_0 = 1/\tau_l$ is the largest relaxation rate of environment equal to the inverse small time cutoff, $\tau_l \ll \tau_{\rm in}$. Diffusion becomes again normal on the time scale $t \gg \tau_h = \tau_l b^{N-1}$, and $\eta_\alpha = \eta_{\rm eff}\tau_h^{\alpha-1}/g_\alpha$, with a proportionality coefficient g_α about unity, $g_\alpha \sim 1$ [71]. For example, $g_\alpha \approx 0.93$, for $\alpha = 0.4$ and $N \geqslant 5$ [72]. The scaling coefficient b controls the quality of approximation of the power law dependence between two time cutoffs. Relative error is about 4% only for a crude decade scaling with $b = 10$, which suffices in most studies, and improves further to 0.01% for $b = 2$ [68]. Interestingly, $\tau_h/\tau_{\rm in} = (\eta_{\rm eff}/\eta_0)^{1/(1-\alpha)}$ independently of b, which makes it possible to estimate the time duration of intermediate subdiffusion in units of $\tau_{\rm in}$ from merely the knowledge of α and an effective enhancement of friction in cytosol relative to that in water in the long-time normal diffusion limit. For example, if $\tau_{\rm in} \sim 1$ ms and $\tilde{\eta}_{\rm eff} = \eta_{\rm eff}/\eta_0 = 10^3$ for $\alpha = 0.5$, intermediate subdiffusion will last until $\tau_h \sim 10^3$ s; i.e., it extends over six time decades in units of $\tau_{\rm in}$. Such a consideration can be very useful for estimating $\tilde{\eta}_{\rm eff}$ from experimental data. We scale time in units of $\tau_{sc} = \eta_0/U_0$. For $U_0 = 10\, k_B T_r$ and for the rod of length $L = 275$ nm consisting of five magnetosomes it is estimated as $\tau_{sc} \approx 0.404$ ms, and for the rod of length 385 nm consisting of seven magnetosomes it is estimated as $\tau_{sc} \approx 0.905$ ms (see Appendix B). This corresponds to the rotational diffusion coefficients $D_0 = 0.248$ rad^2/ms and $D_0 = 0.110$ rad^2/ms, respectively.

C. Relaxation within a potential well

Nonlinear viscoelastic dynamics in a bistable potential is rather intricate [47]. To understand its main features,

it is important to realize first the character of relaxation process in one potential well. This can be done within a parabolic well approximation, $U(\phi) \approx \kappa_{1,2}(\phi - \phi_{\min,1,2})^2/2$, where $\kappa_{1,2} = d^2U(\phi)/d\phi^2|_{\phi=\phi_{\min,1,2}}$. The relaxation of an initial fluctuation, $\delta\phi(0) = \phi(0) - \phi_{\min,1,2}$, within a parabolic potential follows the relaxation law $\langle\delta\phi(t)\rangle = \delta\phi(0)\theta(t)$, with relaxation function $\theta(t)$ whose Laplace transform reads [48,99]

$$\tilde{\theta}(s) = \frac{\tilde{\eta}(s)}{\kappa + s\tilde{\eta}(s)} \tag{12}$$

for arbitrary memory kernel $\eta(t)$. Here we omitted subindexes 1,2 at κ for simplicity. The relaxation function coincides with the normalized *stationary* autocorrelation function of fluctuations, or ACF, $\langle\delta\phi(t_0)\delta\phi(t_0+t)\rangle_{eq}/\langle\delta\phi^2\rangle_{eq}$, with $\langle\delta\phi^2\rangle_{eq} = k_BT/\kappa$, which does not depend on time shift t_0. In other words, the Onsager regression property holds generically within this model, as shown in [99]. However, ACF depends generally on both time arguments and displays aging phenomenon [48,99,100]. In the present case, $\tilde{\eta}(s) = \eta_0 + \eta_\alpha s^{\alpha-1}$, and

$$\tilde{\theta}(s) = \frac{\tau_0 + \tau_r(s\tau_r)^{\alpha-1}}{s\tau_0 + 1 + (s\tau_r)^\alpha} = \frac{r + r_{1-\alpha}s^{\alpha-1}}{s + r + r_{1-\alpha}s^\alpha}, \tag{13}$$

where we denote $\tau_0 = \eta_0/\kappa$, $\tau_r = (\eta_\alpha/\kappa)^{1/\alpha}$ and $r = 1/\tau_0$, $r_{1-\alpha} = \eta_\alpha/\eta_0 = \tau_{\rm in}^{\alpha-1}$. Upon change $\alpha \to 1-\alpha$, i.e., identifying our present α with $1-\alpha$ in [101] and identifying our present τ_0 with $\langle\tau\rangle$ therein, one can see that this result coincides (up to a normalization factor) with one obtained in Ref. [101] for the stationary ACF of fluctuations in a very different model based on the continuous time random walk (CTRW) approach to relaxation phenomena. This other approach is featured by two parallel relaxation channels characterized by normal rate r, and fractional rate $r_{1-\alpha}$, correspondingly, and by a *finite* mean residence time $\langle\tau\rangle = 1/r$; see [75,101] for basic formulations and details. In [101], the corresponding spectral power of fluctuations, $S(\omega)$, and the response function $\chi(\omega)$ are also presented and discussed. The relaxation behavior of $\theta(t)$ depends very strongly on the relationship between τ_0 and τ_r. The time constant τ_r can be expressed through τ_0 and the above $\tau_{\rm in}$ as

$$\tau_r = \tau_0\left(\frac{\tau_0}{\tau_{\rm in}}\right)^{1/\alpha}. \tag{14}$$

A salient feature is that τ_r depends on the potential curvature κ only through τ_0, and $\tau_{\rm in}$ that characterizes free diffusion. The Laplace transform of relaxation function can be inverted exactly to the time domain for a special case $\alpha = 0.5$. Then it reads

$$\begin{aligned}\theta(t) = {} & \frac{1}{2}\left(1 + \frac{1}{\sqrt{1-4z}}\right)e^{(1-\sqrt{1-4z})^2 t/(4z^2\tau_r)} \\ & \times \mathrm{erfc}[(1-\sqrt{1-4z})\sqrt{t/(4z^2\tau_r)}] \\ & + \frac{1}{2}\left(1 - \frac{1}{\sqrt{1-4z}}\right)e^{(1+\sqrt{1-4z})^2 t/(4z^2\tau_r)} \\ & \times \mathrm{erfc}[(1+\sqrt{1-4z})\sqrt{t/(4z^2\tau_r)}],\end{aligned} \tag{15}$$

where $z = \tau_0/\tau_r$, and erfc is the complementary error function. Furthermore, for any $0 < \alpha < 1$, if $\tau_0 \ll \tau_r$, then relaxation follows approximately $\theta(t) \approx E_\alpha[-(t/\tau_r)^\alpha]$; see numerical results in Fig. 4(b) for $\alpha = 0.4$ and the relaxation in the first

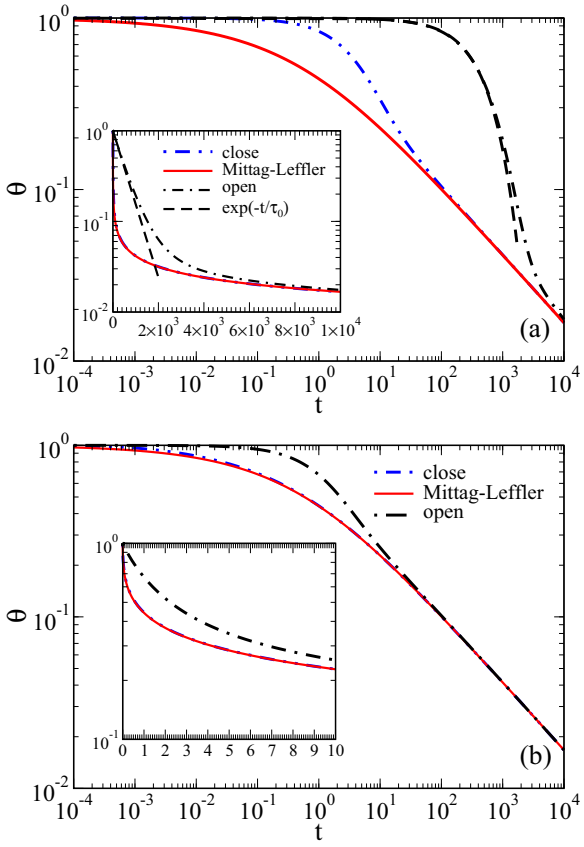

FIG. 4. (Color online) Non-Markovian relaxation function against time in units of τ_r for two different potential wells corresponding to a potential $U(\phi)$ realization in Fig. 2 at $\mu B = 0.3115$ for $\alpha = 0.4$ in parabolic approximation and in neglect of the memory cutoff effects. Time constant τ_r has different absolute values (in units of $\tau_{sc} = \eta_0/U_0$) for different potential wells. Panels (a) and (b) correspond to two different values of fractional friction coefficient $\eta_\alpha \sim \eta_{\rm eff}\tau_h^{\alpha-1}$. In (a), $\tau_h = 10^4$ and $\eta_{\rm eff} = 100\eta_0$, $z_1 = \tau_0/\tau_r = 4.838$ (for the relaxation in the first potential well which corresponds to closed times, see the dash-double-dotted blue curve), and $z_2 = \tau_0/\tau_r = 536.83$ (for the relaxation in the second potential well which corresponds to open times, see the dash-dotted black curve). The dashed black line depicts single-exponential approximation. The solid red curve is the Mittag-Leffler relaxation function $E_\alpha[-(t/\tau_r)^\alpha]$, which corresponds to the Cole-Cole dielectric response and β relaxation in glasslike materials. The tail of relaxation is universally a power law, $\theta(t) \sim t^{-\alpha}$. The inset in (a) shows the same plot on a semilogarithmic scale. It reveals that nearly 70% of initial relaxation in the second well occurs in the exponential regime. In (b), $\eta_{\rm eff}$ is increased to $\eta_{\rm eff} = 1000$, with other parameters kept the same, which corresponds to a tenfold larger η_α, as compare with panel (a). Here $z_1 = 0.015\,93$ (dash-double-dotted blue curve, which is difficult to see because it almost coincides with the solid red line corresponding to the Mittag-Leffler relaxation), and $z_2 = 1.6976$ (dash-dotted black curve). The relaxation in the first potential well is excellently described by the Mittag-Leffler relaxation function, and the relaxation in the second potential well is also clearly nonexponential all the time, as the inset shows. Numerical results are obtained by numerical inversion of the Laplace-transform in Eq. (13) with Stehfest-Gaver method as described in Refs. [102,103].

potential well (closed times), within the parabolic approximation. It is initially a stretched exponential for $t \ll \tau_r$ and then a power law, $\theta(t) \propto t^{-\alpha}$. The spectral power of intrawell fluctuations is $S(\omega) \propto 1/\omega^{1-\alpha}$ at low frequencies, and such an intrawell motion is featured by the Cole-Cole response to external fields [99]. It is measured in many biological tissues [8] and corresponds to the so-called $\beta-$ relaxation in glassy systems. Clearly, for a sufficient small κ and $\tau_{\rm in}$ such a regime can always be realized. Another regime with $\tau_0 \gg \tau_r$ can also be very important. For a given $\tau_{\rm in}$, it can always be realized for a sufficiently large κ, i.e., sufficiently stiff trapping potential. Then the relaxation of $\theta(t)$ starts universally from an exponential regime, $\theta(t) = \exp(-t/\tau_0)$, which changes into a power law tail $\theta(t) \propto 1/t^{\alpha}$; see Fig. 4(a) for $\alpha = 0.4$ (open times) and also Figs. 2 and 3 in [101] for $\alpha = 0.5$. The larger the ratio τ_0/τ_r, the smaller is the weight of a heavy tail. In other words, the major part of $\theta(t)$ relaxation occurs exponentially for $z \gg 1$. The power law tail starts then from some $\theta_c \ll 1$. For example, in Fig. 4(a), about 70% of the whole relaxation in the second potential well (open times) occurs in the exponential regime. The power law tail of open times has just a few percent weight therein, as the main double-logarithmic plot in Fig. 4(a) reveals. Nevertheless, it can be very important yielding to the $S(\omega) \propto 1/\omega^{1+\alpha}$ feature of the fluctuations power spectrum for $\tau_0^{-1} \ll \omega \ll \tau_r^{-1}$. It has been detected, e.g., experimentally in Ref. [60] for transversal fluctuations of cargo moving along a microtubule. Moreover, slow residual relaxation in the potential wells leads generally to a breakdown of the rate theory and validates the physical picture of slowly (on a characteristic time scale of transitions) fluctuating barriers and fluctuating rates.

D. Thermally activated transitions between metastable states of sensor

Although transitions between the potentials wells cannot be described as a rate process for the biophysically most important case of intermediate barriers (less than about 10 k_BT depending on α), in the case of power law memory kernels, the rate theory has been shown to be able to predict, at least in some cases, the most probable logarithm of residence times in the potential wells [47]. Moreover, the rate description is restored in the limit of very high barriers. Then the transition rates $R_{1,2}$ follow as

$$R_{1,2}(\mu) = \frac{\omega_{1,2}}{2\pi}\,\Xi(\mu)\exp(-\beta\Delta U_{1,2}), \tag{16}$$

where $\omega_{1,2} = \sqrt{\kappa_{1,2}/J}$ are circular attempt frequencies, and $0 \leqslant \Xi(\mu) \leqslant 1$ is the so-called transmission coefficient, which for the considered intermediate-to-strong friction limit is found [79,83] as $\Xi(\mu) = \mu/\omega_b$. Here $\omega_b = \sqrt{\kappa_b/J}$ is the imaginary barrier frequency, $\kappa_b = -d^2U(\phi)/d\phi^2|_{\phi=\phi_{\rm max}}$, and μ is the renormalized barrier frequency. The latter one is found at the largest positive root of a transcendental equation taking (in the considered overdamped limit, $J \to 0$) the general form $\mu\tilde{\eta}(\mu) = \kappa_b$, and for the memory kernel considered, $\mu\eta_0 + \eta_\alpha\mu^\alpha = \kappa_b$. By introducing $\tau_0^{(b)} = \eta_0/\kappa_b$ and $\tau_r^{(b)} = (\eta_\alpha/\kappa_b)^{1/\alpha}$, we can write it as

$$\tau_0^{(b)}\mu + \left(\tau_r^{(b)}\mu\right)^\alpha = 1. \tag{17}$$

For the memory kernel expanded into a sum of exponentials it takes the form

$$\mu\left(\eta_0 + \sum_{i=1}^{N}\frac{k_i}{\mu+\nu_i}\right) = \kappa_b, \tag{18}$$

which can be rewritten as an algebraic equation of $N+1$ degree for the unknown μ. For a special case $\alpha = 0.5$, Eq. (17) can be solved exactly to yield $\mu = 4[\tau_r^{(b)}]^{-1}/\left[1+\sqrt{1+4\tau_0^{(b)}/\tau_r^{(b)}}\right]^2$, and

$$R_{1,2} = \frac{1}{2\pi}\sqrt{\frac{\kappa_{1,2}}{\kappa_b}}\frac{1}{\tau_r^{(b)}}\frac{4\exp(-\beta\Delta U_{1,2})}{\left[1+\sqrt{1+4\tau_0^{(b)}/\tau_r^{(b)}}\right]^2}. \tag{19}$$

This insightful result can be expressed in terms of the normal diffusion ($\eta_\alpha \to 0$) overdamped Kramers rate,

$$\begin{aligned} R_{1,2}^{(0)} &= \frac{1}{2\pi}\sqrt{\frac{\kappa_{1,2}}{\kappa_b}}\frac{1}{\tau_0^{(b)}}\exp(-\beta\Delta U_{1,2}) \\ &= \frac{1}{2\pi}\frac{1}{\tau_0^{(b)}}\exp(-\beta\Delta G_{1,2}) \end{aligned} \tag{20}$$

as

$$R_{1,2} = R_{1,2}^{(0)}F\left(z_b = \tau_0^{(b)}/\tau_r^{(b)}\right), \tag{21}$$

where

$$F(z) = \frac{4z}{[1+\sqrt{1+4z}]^2}\,. \tag{22}$$

Notice that in the second line of Eq. (20), we incorporated the difference of the curvatures κ_1 and κ_2 as *additional* entropic contributions to the free energy barriers, $\Delta G_{1,2} = \Delta U_{1,2} - T\Delta S_{1,2}^{(ad)}$ with entropy differences $\Delta S_{1,2}^{(ad)} = k_B\ln(\kappa_{1,2}/\kappa_b)/2$. Generally, reduction of a multidimensional dynamics to a two-state dynamics contains such important additional entropic contributions. It should be mentioned, however, that in our model $U(\phi)$ in Eq. (2) is also temperature dependent, i.e., is in fact a (Gibbs) free energy profile. We consider, however, a fixed value of temperature throughout the paper. The correct separation of $\Delta G_{1,2}$ into the internal energy (or rather enthalpic) part $\Delta H_{1,2}$ and entropic part $-T\Delta S_{1,2}$ must always be done using fundamental thermodynamic relation $\Delta H = \Delta G + T\Delta S = \Delta G - T(\partial\Delta G/\partial T)_P$ [104].

Furthermore, for $z \ll 1$ in (22), $F(z) \approx z$, and for $z \gg 1$, $F(z)$ approaches unity, $F(z) \to 1$. Hence, in the parameter regime $\tau_0^{(b)} \gg \tau_r^{(b)}$, which correlates with $\tau_0 \gg \tau_r$ (see above), $R_{1,2} \approx R_{1,2}^{(0)}$, i.e., the rate is practically not affected by subdiffusion. This is a very important result, which is valid also for other values of α. It is very different from the suppression by the factor $\eta_{\rm eff}/\eta_0$, which some unjustified intuition might suggest. This result shows that subdiffusion does not necessary suppress the activation rates, in accordance with our earlier results in [47] obtained in the presence of inertial effects. Here the inertial effects were, however, entirely neglected. Moreover, it will be shown elsewhere that in the presence of inertial effects the transmission factor for subdiffusive dynamics can arrive at its maximal value of unity in the case of cusplike potential barriers $\kappa_b \gg \kappa_{1,2}$. The combination of nonlinearity

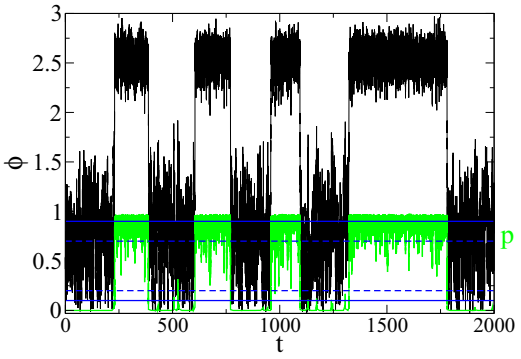

FIG. 5. (Color online) Trajectory realization of Markovian memoryless dynamics. The black line describes stochastic rotational fluctuations of the sensor, while the green (light gray) line depicts fluctuations of the probability of the gate to be open (and normalized ion current fluctuations). The blue horizontal lines depict some detection thresholds (two possible sets are shown). Model parameters: $T = 0.1$, $\mu B = 0.3115$, $\phi_0 = \pi/6$, $\psi = \pi$, $l_{\max} = 1.5$, $f_0 = 1.5$, $l_0 = 1.22$, and $m = 7$ channels in the sensor cluster.

and viscoelastic subdiffusion is really counterintuitive and paradoxical. An essential suppression of rate occurs in the regime $\tau_0^{(b)} \ll \tau_r^{(b)}$, which correlates with $\tau_0 \ll \tau_r$, i.e., when the Mittag-Leffler relaxation within potential wells covers most of time. Then we obtain (for arbitrary α)

$$R_{1,2} \approx \frac{1}{2\pi}\sqrt{\frac{\kappa_{1,2}}{\kappa_b}}\frac{1}{\tau_r^{(b)}}\exp(-\beta\Delta U_{1,2}). \tag{23}$$

Notice that it is smaller than $R_{1,2}^{(0)}$ by the factor $\tau_0^{(b)}/\tau_r^{(b)}$.

III. RESULTS

A. Markovian dynamics

We performed first stochastic simulations of Markovian memoryless dynamics ($\eta_\alpha \to 0$) for the same parameters as in Figs. 2 and 3, $\psi = \pi$, with time step $\delta t = 2 \times 10^{-6}$ using the stochastic Heun method, in accordance with our previous studies. A typical trajectory of bistable fluctuations for $\mu B \approx 3.12\, k_B T_r$ is shown in Fig. 5. One can see characteristic bistable fluctuations of sensor orientation. It flips between two metastable positions (interwell fluctuations) and exhibits also profound fluctuations within potential wells (intrawell fluctuations). The open-shut dynamics reveals a new flickering feature, apart from large amplitude fluctuations reflecting bistability of sensor. Flickering comes about from intrawell fluctuations of sensor corresponding to its open metastable state; see below.

The statistics of transitions can be determined from one very long single trajectory by setting different detection thresholds, e.g., $p_1 = 0.2$ and $p_2 = 0.7$ (set 1), or $p_1 = 0.1$ and $p_2 = 0.9$ (set 2). One can also relate thresholds to the minima of $U(\phi)$ (set 3). For example, for $\mu B = 0.3115$ in Fig. 2, $\phi_{\min,1} \approx 0.762 \approx 43.69^\circ$, $\phi_{\min,2} \approx 2.551 \approx 146.13^\circ$, and for $\mu B = 0.4363$ in Fig. 2, $\phi_{\min,1} \approx 0.910 \approx 52.14^\circ$, $\phi_{\min,2} \approx 2.559 \approx 146.63^\circ$. With this choice, $\phi_{\min,1}$ corresponds to a very small $p_1 \sim 10^{-8}$–10^{-6}, and $\phi_{\min,2}$ corresponds to $p_2 \sim 0.92$–0.95. Yet an experimentalist can prefer the choice $p_1 = 0.5$ and some $p_2 > p_1$, e.g., $p_2 = 0.9$ (set 4). It must be emphasized that the statistics of transitions can very essentially depend on the thresholds, i.e., on how the current signal is detected. This is because there are very fast events even within the purely Markovian version of the considered dynamics, where very short outbursts occur from the open state to the closed state, when the probability of the channel to be open becomes briefly less than one-half. The lower the low detection threshold $0 < p_1 \leqslant 0.5$ in Fig. 5, the larger is the number of missed short closure events. This is why the averaged residence times in the states do increase with lowering p_1, when the bursting events are increasingly disregarded. The explanation of a highly bursting character of dynamics even in the absence of memory effects can easily be grasped from Fig. 2. Indeed, the maximum of the potential $U(\phi)$ corresponds to the opening probability $p \sim 0.17$–0.27, depending on the μB value in Fig. 2. Hence, an essential part of closure dynamics occurs when the sensor moves within the second metastable minimum of sensor not reaching the transition state of sensor. This observation is also quite generally of a great importance within the context of gating dynamics of other ionic channels. It emphasizes the importance of a very complex molecular structure of ionic channels [105], where the sensory part and the gating part are generally not the same and their mechanical coupling can be very important in all fine details. Our treatment makes this implicit complexity quite obvious within the simplest model setting. The opening probability of the channel defined as a time average, $p = \langle\tau_o\rangle/(\langle\tau_o\rangle + \langle\tau_c\rangle)$, however, is weakly sensitive to the choice of the detection thresholds and agrees reasonably well with the ensemble averaged result depicted in Fig. 3, where $p \approx 0.52$ at $\mu B = 0.3115$ and $\psi = \pi$.

Transitions from open to closed state are regarded as accomplished by a downward crossing of the low threshold. In turn, transitions from closed to open state are accomplished by an upward crossing of the high threshold. In this way, one finds pairs of random time intervals in the closed, τ_c, and open, τ_o, states whose statistics is subsequently studied. For a very long trajectory of the kind depicted in Fig. 5, the survival probabilities $P_o(\tau)$ and $P_c(\tau)$, which correspond to residence time distributions, $\psi_i(\tau) = -dP_i(\tau)/\tau$, $i = o,c$, are shown in Figs. 6(a)–6(d). They are derived from the same single very long trajectory by using different sets of thresholds. As a test of ergodicity (in distribution), we derived probability density $\hat{P}(\phi)$ of sensor orientations from a single trajectory and compared it with the ensemble equilibrium $P_{\rm eq}(\phi) \propto \exp[-U(\phi)/(k_B T)]$. Excellent agreement (not presented) implies ergodicity. In Fig. 6, we provide fits of the tail of distributions with the exponential functions $c_i \exp(-\tau/\tau_i)$, with weight c_i and time constant τ_i. Furthermore, the initial part of closed time distribution therein is nicely fitted by the fourth type Pareto law with survival probability [106],

$$P(\tau) = \frac{1}{[1 + (\tau/\tau_p)^{\gamma_1}]^{\gamma_2}}\,. \tag{24}$$

For $\tau \gg \tau_p$, $P(\tau) \propto \tau^{-\gamma}$, with $\gamma = \gamma_1\gamma_2$. It reflects the short time bursting dynamics. Notice that in Fig. 6(a) the open time distribution is almost a single exponential, $c_o \approx 0.966$, while the weight of the exponential tail of closed time distribution

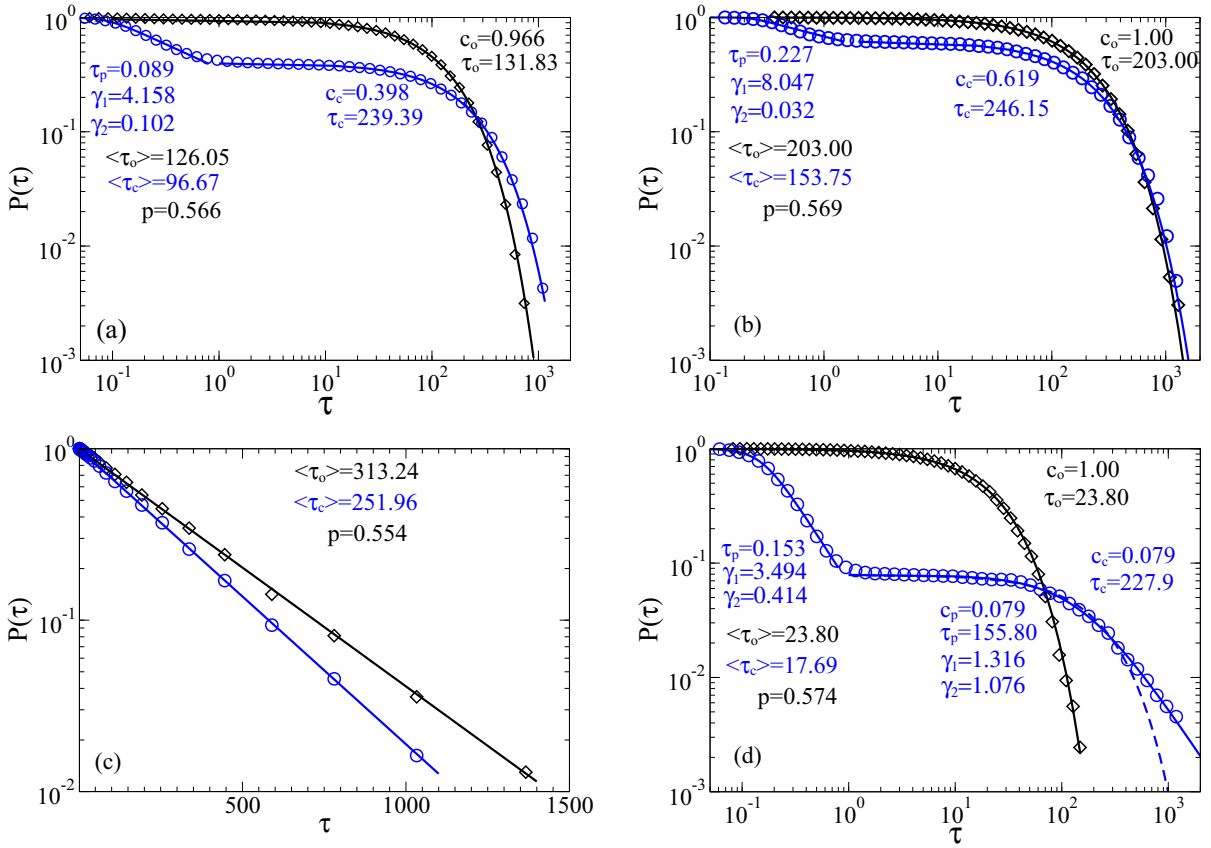

FIG. 6. (Color online) Survival probabilities of open (black diamonds) and closed (blue open circles) times derived from numerical data for the case $\mu B = 0.3115$, $\psi = \pi$, $\phi_0 = \pi/6$, using different sets of detection thresholds: (a) $p_1 = 0.2$, $p_2 = 0.7$; (b) $p_1 = 0.1$, $p_2 = 0.9$, (c) for the minima of $U(\phi)$ used as detection thresholds, $p_1 = p(\phi_{\min,1})$, $p_2 = p(\phi_{\min,2})$; (d) $p_1 = 0.5$, $p_2 = 0.9$. Lines present the corresponding exponential, $c_i \exp(-\tau/\tau_i)$, or Pareto law (24) fits with the parameters shown in the plots. The mean residence times, as well as the opening probability $p = \langle\tau_o\rangle/(\langle\tau_o\rangle + \langle\tau_c\rangle)$ are also shown. Notice a strong dependence of these fits on the detection thresholds used. Other parameters: $T = 0.1$, $I_{\max} = 1.5$, $f_0 = 1.5$, $r_0 = 1.22$, and $m = 7$ channels in the sensor cluster.

is about $c_c \approx 0.4$ only, and nearly 60% of distribution is described by the Pareto law (24). With lowering the detection threshold p_1 in Fig. 6(b) to $p_1 = 0.1$, the weight of exponential tail increases to $c_c \approx 0.62$. This is because fewer bursting events are detected. The variation of the time constant τ_c describing mean residence time in the closed state with a variation of detection thresholds in Figs. 6(a)–6(c) is not statistically significant. Notice that a two-stage relaxation of the closed times $P(\tau)$ cannot be described by a simple sequential Markovian scheme with just two closed substates, $C_2 \leftrightarrow C_1 \rightarrow O$. This is because (i) the relative weight of two stages depends very essentially on the detection threshold and (ii) initial stage is described by the Pareto power law (24) and not by an exponential.

Furthermore, if to detect transitions by crossing $p_{1,2}$ levels corresponding to the minima of $U(\phi)$ (set 3), then the survival probabilities become practically single exponential [see Fig. 6(c)], where the mean times coincide with the corresponding time constants. In this case, the bursts within long opening events are completely neglected. The mean residence times increase accordingly. The standard Kramers rate result in (20) gives $R_1^{(0)} \approx 0.003\,805\,2$ and $R_2^{(0)} \approx 0.003\,089\,9$. The corresponding inverse values $1/R_1^{(0)} \approx 262.80$ and $1/R_2^{(0)} \approx 323.63$ agree with $\langle\tau_c\rangle \approx 251.96$ and $\langle\tau_o\rangle \approx 313.24$, correspondingly, in Fig. 6(c) within a 4% error margin. This is a typical accuracy of our stochastic simulations. However, if to use $p_1 = 0.5$ for the lower threshold, which experimentalists can prefer, and to keep $p_2 = 0.9$, a more complex picture emerges for the closed residence times; see Fig. 6(d). It reveals two characteristic power law regimes described by Pareto laws. The initial Pareto law describes almost 90% of the probability decay with $\gamma = \gamma_1\gamma_2 = 1.405$. It corresponds to the residence time distribution $\psi(\tau) \propto \tau^{-\delta}$, with $\delta = 1 + \gamma = 2.405$. Interestingly, similar power laws were indeed derived from experimental recordings of large conductance BK ion channels [40], which resemble the open-shut dynamics in our Fig. 5. However, a very different phenomenological theory has been proposed earlier for such a gating dynamics [46]. The second Pareto law part (24) in Fig. 6(d) has weight $c_p \approx 0.079$ and describes thus about the last 8% of decay. Unexpectedly, an exponential tail fit of the data for the closed times in Fig. 6(d) is worse, although its time constant correlates with one in Fig. 6(c), as expected. The distribution of open times remains, however, practically single exponential independently of thresholds with a threshold-dependent time constant. Our results show that a continuous-state Markovian bistable dynamics can

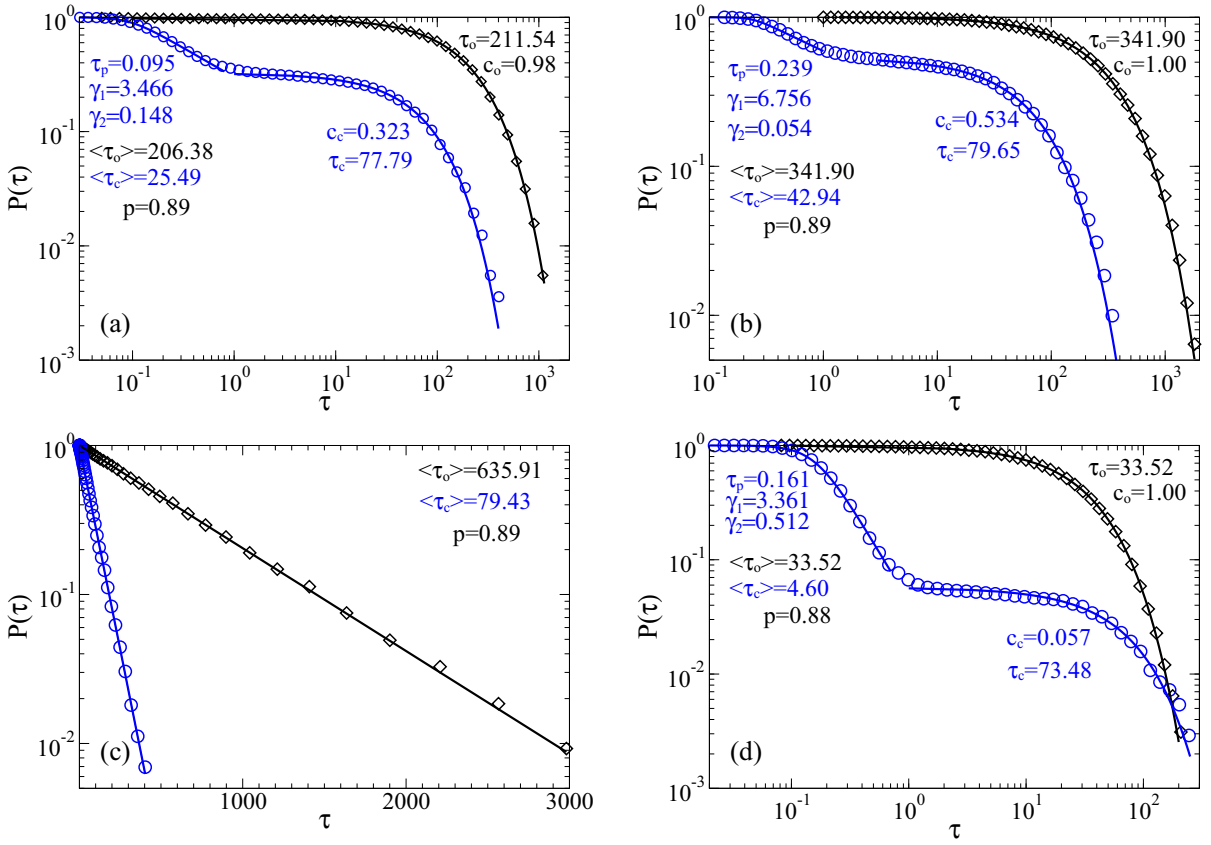

FIG. 7. (Color online) Survival probabilities of open (black diamonds) and closed (blue open circles) times derived from numerical data for the case $\mu B = 0.4363$, $\psi = \pi$ using different sets of detection thresholds: (a) $p_1 = 0.2$, $p_2 = 0.7$; (b) $p_1 = 0.1$, $p_2 = 0.9$, (c) for the minima of $U(\phi)$ used as detection thresholds, $p_1 = p(\phi_{\min,1})$, $p_2 = p(\phi_{\min,2})$; (d) $p_1 = 0.5$, $p_2 = 0.9$. Lines present the corresponding exponential, $c_i \exp(-\tau/\tau_i)$, and the Pareto law (24) fits with the parameters shown in the plots. The mean residence times, as well as the opening probability $p = \langle\tau_o\rangle/(\langle\tau_o\rangle + \langle\tau_c\rangle)$ are also displayed. Notice a strong dependence of these fits on the detection thresholds used. Other parameters: $T = 0.1$, $l_{\max} = 1.5$, $f_0 = 1.5$, $r_0 = 1.22$, and $m = 7$ channels in the sensor cluster.

explain such experimental non-Markovian features (within a contracted two-state non-Markovian dynamics) as bursting and power law distributions of the residence times. They can be caused by a nontrivial interplay of coupled sensor and gate dynamics, as well as threshold levels used for detection. What we measure depends really on how we detect. This is a signature of complex dynamics. Notice that the opening probability within the two-state interpretation of continuous state dynamics is rather robust with respect to the choice of the detection thresholds. It agrees fairly with the ensemble average in (3) done for the continuous-state dynamics.

With increasing the number of magnetosomes in the sensor rod to $n = 7$ (or for a correspondingly larger single nanoparticle used as sensor), the probability of channels to be open in the magnetic field of Earth increases to over $p = 0.8$ at a proper field orientation; see Fig. 3. The residence times statistics displays similar features; see Figs. 7(a)–7(d). Namely, the open times are nearly exponentially distributed, whereas the distribution of closed times depends strongly on the lower detection threshold. The lower the threshold, the closer the distribution is to a single exponential. The rate theory yields $R_1^{(0)} \approx 0.012\,306$, and the corresponding $1/R_1^{(0)} \approx 81.26$ agrees well, within a 2.25% error margin, with the numerical value of mean close time $\langle\tau_c\rangle \approx 79.43$ in Fig. 7(c). For the corresponding open times, the rate theory yields $1/R_2^{(0)} \approx 708.11$, which agrees in this case somewhat worse, within a 10.2% error margin, with numerical $\langle\tau_o\rangle \approx 635.91$ in Fig. 7(c). However, experimentalists can reveal power law features related to bursting, if they set $p_1 = 0.5$ or somewhat lower. So, in Fig. 7(d) Pareto law with $\gamma = \gamma_1\gamma_2 \approx 1.721$ covers about 94% of the survival probability decay of the closed time distribution, which ends by an exponential tail with the weight of about 5.7% and decay time constant τ_c, which weakly depends on the choice of threshold; see Figs. 7(a) to 7(d). The Pareto law describes durations of closed time intervals within a burst, whereas the time constant τ_c corresponds approximately to the mean time interval between the bursts, when the channels are well closed. Clearly, the time constant of open times τ_o depends very essentially on the choice of lower detection threshold.

Our results show that if the sensor motion would occur in water, its dynamics would be reasonably fast, being in hundreds of milliseconds range. Hence, it could serve as a detector for quasistatic or slowly changing magnetic fields. However, in cytosol the effective friction η_{eff} is enhanced dramatically for the particles of a typical size of magnetosomes.

Kirschvink *et al.* estimated $\tilde{\eta}_{\rm eff} = \eta_{\rm eff}/\eta_0$ by a factor of $\tilde{\eta}_{\rm eff} = 100$ [12,21]. If to just renormalize the Stokes friction by this factor, the effective time scale $\tau_{\rm sc}$ would enlarge accordingly, $\tau_{\rm sc} \to (\tilde{\eta}_{\rm eff} + 1)\tau_{\rm sc}$. Then our sensor would be really too slow to be functional. However, accounting for non-Markovian memory effects by a naive renormalization of the friction coefficient is patently wrong within the context of thermally activated dynamics, as it is well recognized within non-Markovian generalizations of Kramers rate theory [79–83]. Therefore, it is compelling to clarify the role of low-dimensional non-Markovian memory effects.

B. Role of memory effects

Stochastic simulations of Eq. (9) were done for the following additional parameters: $\alpha = 0.4$ [59,60,72,73], $\nu_0 = 10^4$, $N = 9$, and $b = 10$. Hence, $\tau_l = 10^{-4}$ and $\tau_h = 10^4$. The latter time is about 4.04 s for $\tau_{\rm sc} \approx 0.404$ ms or about 9.05 s for $\tau_{\rm sc} \approx 0.905$ ms. Furthermore, we used two values of $\eta_{\rm eff}$, $\eta_{\rm eff} = 100$ and $\eta_{\rm eff} = 1000$, which correspond to two different values of $\eta_\alpha = \eta_{\rm eff}\tau_h^{\alpha-1}/g_\alpha$ in simulations, and the rotational subdiffusion coefficients $D_\alpha \approx 0.360$ rad^2/ms$^{0.4}$ and $D_\alpha \approx 0.036$ rad^2/ms$^{0.4}$ at $\tau_{\rm sc} \approx 0.404$ ms or $D_\alpha \approx 0.260$ rad^2/ms$^{0.4}$ and $D_\alpha \approx 0.026$ rad^2/ms$^{0.4}$ at $\tau_{\rm sc} \approx 0.905$ ms, respectively. In this respect, one can enlarge both $\eta_{\rm eff}$ and τ_h (by using a larger N), while keeping η_α the same. For example, by taking $N = 11$, and enlarging τ_h to about 404 and 905 s, correspondingly, we can keep η_α the same by enlarging $\eta_{\rm eff}$ from 100 to approximately 1585 and from 1000 to approximately 15 850, respectively. Furthermore, for the used parameters we have $\tau_{\rm in} \approx 4.64$ for $\eta_{\rm eff} = 100$ and $\tau_{\rm in} \approx 0.01$ for $\eta_{\rm eff} = 1000$. For $\tau_{\rm sc} \approx 0.404$ ms, this corresponds to $\tau_{\rm in} \approx 1.88$ ms ($\eta_{\rm eff} = 100$) or $\tau_{\rm in} \approx 0.04$ ms ($\eta_{\rm eff} = 1000$). Furthermore, for $\tau_{\rm sc} \approx 0.905$ ms, this corresponds to $\tau_{\rm in} \approx 4.20$ ms ($\eta_{\rm eff} = 100$) or $\tau_{\rm in} \approx 0.09$ ms ($\eta_{\rm eff} = 1000$).

The first striking universal feature of the influence of viscoelastic memory effects is the emergence of a stretched exponential distribution $c_i \exp[-(\tau/\tau_i)^{\beta_i}]$,$0 < \beta_i < 1$ out of a formerly exponential one; compare Fig. 6(c) and Fig. 8(a), where $\eta_{\rm eff} = 100$, for other parameters being the same in both figures and detection thresholds set at the minima of $U(\phi)$. In Fig. 8(a), the residence time distributions (RTDs) become stretched exponential (Weibull distribution) to a good degree, $c_o \approx 1$, $c_c \approx 1$, except for some initial times; see in the inset, where a deviation from linear dependence of $-\ln P(\tau) \propto (\tau/\tau_i)^{\beta_i}$ plotted on the double-logarithmic scale becomes seen. For this choice of thresholds, we can compare the results of non-Markovian rate theory (NMRT), namely the Grote-Hynes result in Eqs. (16) and (17), with our numerics for the particular memory kernel studied. As observed in Ref. [47], the Grote-Hynes result is capable of describing the most probable value of the logarithmically transformed residence times, $\ln\tau$, even beyond the strict rate regime, when RTDs become profoundly nonexponential. For the case of Weibull distribution characterized by the survival probability $P_i(\tau) = \exp[-(\tau/\tau_i)^{\beta_i}]$ and non-Markovian rate $R(\tau) = -d\ln P(\tau)/d\tau = \beta_i \tau_i^{-1}/(\tau/\tau_i)^{1-\beta_i}$, the correspondingly transformed distribution of $y = \ln\tau$ has its maximum at $y_{\rm max} = \ln\tau_i$. Hence, in accordance with [47], NMRT is expected to yield τ_i of Weibull distribution as $\tau_i = R_i^{-1}$. For the results depicted in Fig. 8(a), the Grote-Hynes result

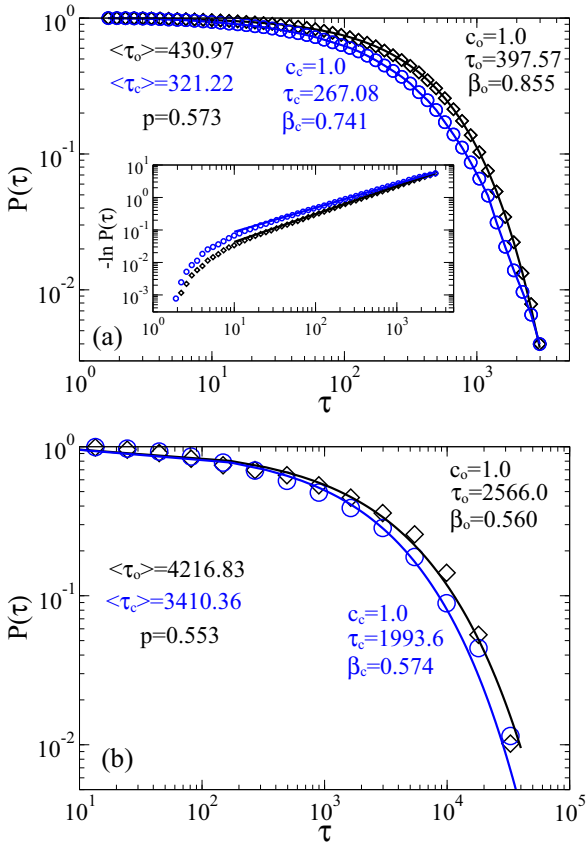

FIG. 8. (Color online) Survival probabilities of open (black diamonds) and closed (blue open circles) times derived from numerical data for the case $\mu B = 0.3115$, $\psi = \pi$, using the detection thresholds defined by the minima of $U(\phi)$, $p_1 = p(\phi_{\min,1})$, $p_2 = p(\phi_{\min,2})$ for (a) $\eta_{\rm eff} = 100$ and (b) $\eta_{\rm eff} = 1000$. Lines present the corresponding stretched exponential, $c_i \exp[-(\tau/\tau_i)_i^\beta]$, fits with the parameters shown in the plots. The mean residence times, as well as the opening probability $p = \langle\tau_o\rangle/(\langle\tau_o\rangle + \langle\tau_c\rangle)$, are also displayed. Other parameters: $T = 0.1$, $l_{\rm max} = 1.5$, $f_0 = 1.5$, $l_0 = 1.22$, and $m = 7$ channels in the sensor cluster.

yields $R_i = 0.8169\ R_i^{(0)}$, for the exact memory kernel, where $R_i^{(0)}$ is the overdamped Kramers result. It has been already discussed above in relation to our numerical results presented in Fig. 6(c). Hence, NMRT yields $\tau_{o,\rm exact}^{(\rm NMRT)} \approx 396.17$ and $\tau_{c,\rm exact}^{(\rm NMRT)} \approx 321.70$ for the exact memory kernels. For the memory kernels approximated by a sum of exponentials, we obtain $\tau_o^{(\rm NMRT)} \approx 395.30$, $\tau_c^{(\rm NMRT)} \approx 321.00$. Notice that the kernel approximation introduces an error of about 0.2% only in theoretical NMRT results. The value $\tau_{o,\rm exact}^{(\rm NMRT)} \approx 396.17$ agrees very well with $\tau_o = 397.57$ in Fig. 8(a). The difference is less than 0.4%. Furthermore, $\tau_{c,\rm exact}^{(\rm NMRT)} \approx 321.70$ somewhat overestimates numerical $\tau_c \approx 267.08$. However, it agrees well with the numerical average $\langle\tau_c\rangle \approx 321.22$. Also for the results in Fig. 8(b), where we increase $\eta_{\rm eff}$ to $\eta_{\rm eff} = 1000$, for the same other parameters, NMRT yields $\tau_{o,\rm exact}^{(\rm NMRT)} \approx 2531.56$ and $\tau_{c,\rm exact}^{(\rm NMRT)} \approx 2055.68$ for the exact memory kernels and $\tau_o^{(\rm NMRT)} \approx 2450.84$ and $\tau_c^{(\rm NMRT)} \approx 1990.13$ for the approximate kernels. The error due to the memory kernel

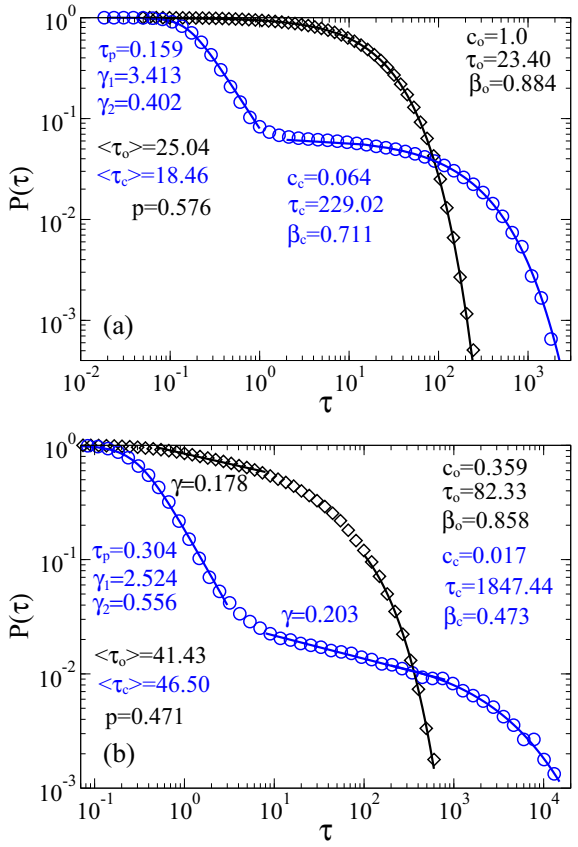

FIG. 9. (Color online) Survival probabilities of open (black diamonds) and closed (blue open circles) times derived from numerical data for the case $\mu B = 0.3115$, $\psi = \pi$, using the detection thresholds $p_1 = 0.5$ and $p_2 = 0.9$ for (a) $\eta_{\rm eff} = 100$ and (b) $\eta_{\rm eff} = 1000$. Lines present the corresponding stretched exponential, $c_i \exp[-(\tau/\tau_i)_i^{\beta}]$, Pareto law (24), and power law, $\sim \tau^{-\gamma}$, fits with the parameters shown in the plots. The mean residence times, as well as the opening probability $p = \langle\tau_o\rangle/(\langle\tau_o\rangle + \langle\tau_c\rangle)$, are also displayed. Other parameters: $T = 0.1$, $l_{\max} = 1.5$, $f_0 = 1.5$, $l_0 = 1.22$, and $m = 7$ channels in the sensor cluster.

approximation now increases to about 3.2%. $\tau_{o,\rm exact}^{(\rm NMRT)} \approx 2531.56$ agrees with $\tau_o \approx 2566.0$ derived from the numerical data using maximum likelihood fitting within 1.4% error margin. Also $\tau_{c,\rm exact}^{(\rm NMRT)} \approx 2055.68$ agrees with the maximum likelihood value $\tau_c \approx 1993.6$ within a 3% error margin. Notice that deviation from the numerical mean values, $\langle\tau_o\rangle \approx 4216.83$ and $\langle\tau_c\rangle \approx 3410.36$, in this case is very essential. In this respect, NMRT describes the most probable $\ln\tau$ generally much better than the mean residence time $\langle\tau\rangle$. Only in the strict rate regime or for β_i close to one does NMRT describe well $\langle\tau\rangle$, which coincides with the effective inverse rate thus defined and is also the so-called stationary flux-over-population rate [83]. Our results confirm that NMRT is of a high predictive value even beyond the strict rate regime [47,48]. What it cannot do, however, is predict the form of nonexponential RTDs, or detailed course of non-Markovian kinetics.

Furthermore, in Fig. 9 the results are depicted for the same anomalous kinetics discussed in Fig. 8, but for the detection thresholds $p_1 = 0.5$ and $p_2 = 0.9$ (set 4). For the smaller value of η_α in Fig. 9(a), one can see, by comparison with Fig. 6(d), that the initial Pareto law for the closed times is not changed dramatically. This is because on the corresponding initial time scale dynamics is nearly normal. The profound changes are reflected by the tail of the closed time survival probability and by the whole open time distribution, which are stretched exponential. The average residence times are only slightly enlarged. However, with the increase of η_α some further changes become detectable in Fig. 9(b). Namely, the mean residence times increase, which is expected, however, not so strongly as for another detection threshold choice; compare with Fig. 8(b). Next, an initial power law regime can be revealed in the distribution of open times, and the weight of a stretched exponential tail is only $c_o \approx 0.359$ versus $c_o \approx 1$ in Fig. 9(a), where the stretched exponential covers practically over all essential transition times [except for very short times; see the inset in Fig. 8(a)]. Also, an intermediate power law emerges for closed times in Fig. 9(b), and the weight of the stretched exponential tail becomes smaller: $c_c \approx 0.017$ in Fig. 9(b) vs $c_c \approx 0.064$ in Fig. 9(a). Moreover, the initial Pareto law is also changed in Fig. 9(b). This is because for larger $\eta_{\rm eff} = 1000$ diffusion is not normal anymore on the related time scale. Similar characteristic features hold also for other choices of thresholds, see the Supplemental Material [107].

For the same detection thresholds, but a larger $\mu B = 0.4163$ the results are depicted in Figs. 10(a) and 10(b). These results are to be compared with the results in Fig. 7(d), in the absence of non-Markovian effects. Again, for a smaller η_α ($\eta_{\rm eff} = 100$), the mean residence times are almost not influenced, although the initial power law parameters in the survival probability of closed tomes are somewhat changed. The most essential typical change is the conversion of exponential RTD of open times and an exponential tail of the closed time distribution into the stretched exponential dependencies. The larger η_α in Fig. 10(b) leads to expectedly larger mean residence times and smaller β_i of stretched exponential tails. Notice also the emergence of an intermediate power law for the closed times and an initial power law regime for the open times. Furthermore, survival probabilities corresponding to the thresholds set in accordance with the $U(\phi)$ minima are shown in Fig. 11. They are clearly stretched exponentials in Fig. 11(a) with the parameters derived using the maximum likelihood criterion. In this case, NMRT predicts $\tau_{o,\rm exact}^{(\rm NMRT)} \approx 887.93$ and $\tau_{c,\rm exact}^{(\rm NMRT)} \approx 101.90$ for the exact memory kernels and $\tau_o^{(\rm NMRT)} \approx 885.68$, $\tau_c^{(\rm NMRT)} \approx 101.64$ for the approximate ones. $\tau_{o,\rm exact}^{(\rm NMRT)}$ agrees with the numerical $\tau_o \approx 833.8$ within a 6.1% error margin, while the agreement of $\tau_{c,\rm exact}^{(\rm NMRT)}$ with the numerical $\tau_c \approx 92.84$ is worse, with about 8.9% discrepancy. Interestingly, in this case the mean values, $\langle\tau_o\rangle \approx 883.38$ and $\langle\tau_o\rangle \approx 107.73$ agree with the results of NMRT theory better, within 0.51% and 5.72% error margins for the exact memory kernels. This shows that for larger β_i, like $\beta_0 = 0.883$ and $\beta_c = 0.788$, in this plot the difference between τ_i determined from the most probable $\ln\tau_i$ and the corresponding mean values $\langle\tau_i\rangle$ can be within the actual statistical errors of our simulations. In Fig. 11(b), the results for $\eta_{\rm eff} = 1000$ are presented at the same other parameters. In this figure, a maximum likelihood fit by a stretched exponential with $\beta_0 \approx 0.549$ and $\tau_o \approx 5.917 \times 10^3$ is shown for the open time

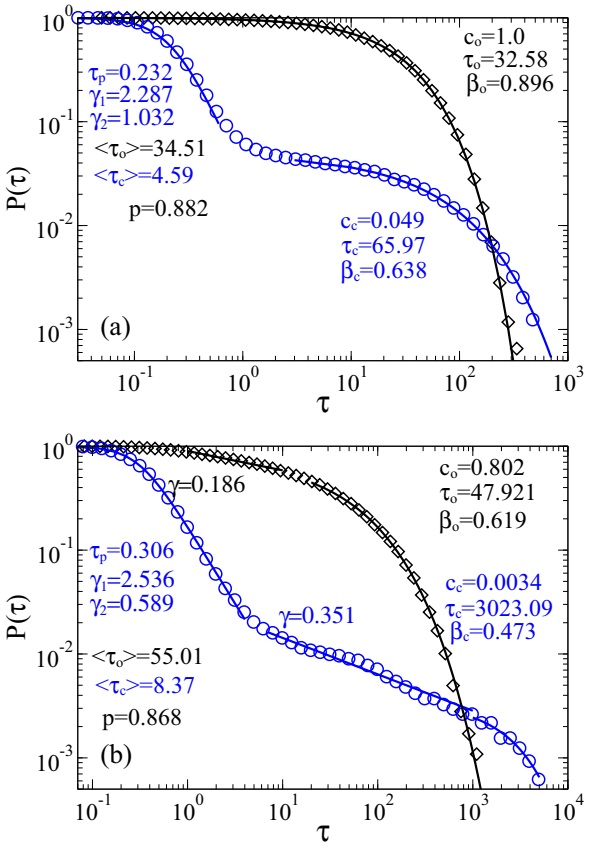

FIG. 10. (Color online) Survival probabilities of open (black diamonds) and closed (blue open circles) times derived from numerical data for the case $\mu B = 0.4346$, $\psi = \pi$, using the detection thresholds $p_1 = 0.5$ and $p_2 = 0.9$ for (a) $\eta_{\text{eff}} = 100$ and (b) $\eta_{\text{eff}} = 1000$. Lines present the corresponding stretched exponential, $c_i \exp[-(\tau/\tau_i)_i^{\beta}]$, Pareto law (24), and power law, $\sim\tau^{-\gamma}$, fits with the parameters shown in the plots. The mean residence times, as well as the opening probability $p = \langle\tau_o\rangle/(\langle\tau_o\rangle + \langle\tau_c\rangle)$ are also displayed. Other parameters: $T = 0.1$, $l_{\max} = 1.5$, $f_0 = 1.5$, $l_0 = 1.22$, and $m = 7$ channels in the sensor cluster.

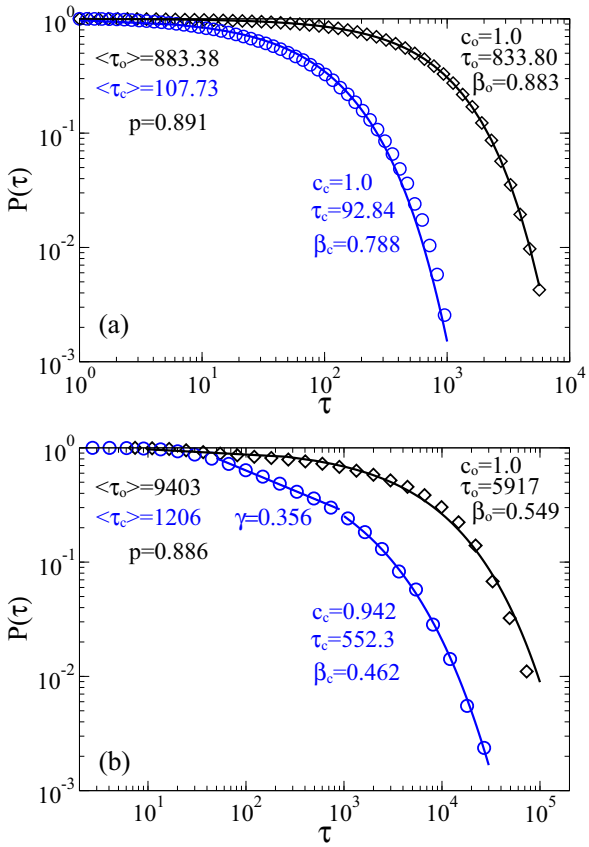

FIG. 11. (Color online) Survival probabilities of open (black diamonds) and closed (blue open circles) times derived from numerical data for the case $\mu B = 0.4363$, $\psi = \pi$, using the detection thresholds defined by the minima of $U(\phi)$, $p_1 = p(\phi_{\min,1})$, $p_2 = p(\phi_{\min,2})$ for (a) $\eta_{\text{eff}} = 100$ and (b) $\eta_{\text{eff}} = 1000$. Lines present the corresponding stretched exponential, $c_i \exp[-(\tau/\tau_i)_i^{\beta}]$, and power law fits with the parameters shown in the plots. The mean residence times are also shown along with the opening probability $p = \langle\tau_o\rangle/(\langle\tau_o\rangle + \langle\tau_c\rangle)$. Other parameters: $T = 0.1$, $l_{\max} = 1.5$, $f_0 = 1.5$, $l_0 = 1.22$, and $m = 7$ channels in the sensor cluster.

distribution. The closed time kinetics is more complex. It reveals an intermediate power law, $\gamma \approx 0.356$, and a stretched exponential tail and therefore is not expected to be described by NMRT. Let us compare the analytical NMRT results with the numerical results depicted in Fig. 11(b). NMRT yields $\tau_{o,\text{exact}}^{(\text{NMRT})} \approx 6.817 \times 10^3$ and $\tau_{c,\text{exact}}^{(\text{NMRT})} \approx 0.782 \times 10^3$ for the exact memory kernels and $\tau_o^{(\text{NMRT})} \approx 6.553 \times 10^3$ and $\tau_c^{(\text{NMRT})} \approx 0.752 \times 10^3$ for the approximate memory kernels used in simulations. The error introduced by the memory kernel approximation is about 3.9% in this case. The numerical mean values obtained on 1267 transitions (which required about 9 weeks of simulations), $\langle\tau_o\rangle \approx 9.403 \times 10^3$ and $\langle\tau_c\rangle \approx 1.207 \times 10^3$, are larger than $\tau_{o,c}^{(\text{NMRT})}$ by 43.5% and 60.5%, correspondingly. At the same time, the maximum likelihood value $\tau_o \approx 5.917 \times 10^3$ deviates from $\tau_o^{(\text{NMRT})}$ by about 6.6% only. However, NMRT clearly fails to describe characteristic features of the closed time distribution, which has a significant power law part. Two-dimensional densities corresponding to Fig. 11(a) and Fig. 11(b) in the Supplemental Material [107] (see Figs. 3 and 4 therein, respectively) provide some important additional insight in this respect.

IV. DISCUSSION

We generalized a gating spring model of ion channels open-shut dynamics originally proposed for ion channels in stereocilia of hair cells [34] in application to hypothetical ion channels involved in magnetosensing [12]. Our modeling displays several generic features beyond the particular model considered. This makes it pertinent to other ionic channels in living cells, where a generalized coordinate of gating variable and sensor can be very different. For example, the sensor is presented by charged α helices in the case of voltage-sensitive ion channels [105]. The first striking generic feature is that the sensor moves typically in a viscoelastic environment, rather than a simple fluidlike medium. In the present model this is cytosol. However, it can also be a biological membrane or ion channel protein macromolecule itself, with a sensory part relocating inside the macromolecule. We showed that viscoelasticity alone can explain the physical

origin of stretched exponential and power law distributions of open and shut residence times. As a matter of fact, they emerge already within a standard double-well description of the sensor energetics with well defined potential wells, rather than due to a flat or rugged free energy landscape (another possibility). The neglect of the medium's viscoelasticity leads immediately to distinct single-exponential distributions of the sensor residence times within our model; see Figs. 6(c) and 7(c). Hence, viscoelasticity can be the primary physical reason of complex nonexponential gating dynamics, the explanation, which has apparently been overlooked thus far. Second, we treat the gating spring elasticity within a nonlinear FENE model, where a maximal extension length of the linker is taken into account. It is more physical than a standard harmonic spring model. Next, the probability $p(\phi)$ of a channel to be open does not reflect one-to-one the characteristic features of the sensor potential $U(\phi)$. This is, in fact, a generic feature of the gating spring model, which is not related in principle to viscoelasticity or nonlinear elastic effects. However, this fundamental feature has also been overlooked earlier. In our model, the value $p(\phi) = 0.5$ when the channel is half open belongs to the attraction domain of sensor open state, rather than to the potential barrier (transient state) separating two domains of attraction, and the barrier value $p_b = p(\phi_{\max})$ can be as small as $p_b \sim 0.1$, depending on μB and ψ. Even in the Markovian memoryless case, this leads to a profoundly bursting character of the ion current recordings reflecting $p[\phi(t)]$ fluctuations within the open state of the sensor; see Fig. 5. Theorists can believe that the most rigorous way to calculate the RTDs in open and closed states of a channel is to use the detection thresholds placed at the minima of $U(\phi)$. For a purely Markovian dynamics such a procedure leads to single-exponential distributions of residence times of the *sensor* [see Figs. 6(c) and 7(c)], with the mean residence times given by the inverse of Kramers rate. However, experimentalists can proceed differently. After detecting a bursting character of *ion current* fluctuations, like in our Fig. 5, an experimentalist is expected to put one detection threshold at $p_1 = 0.5$ and another one somewhere at $p_2 > p_1$ [108], e.g., at $p_2 = 0.9$, as in our Figs. 6(d) and 7(d). Then he or she would find a Pareto distribution (24) of closed residence times within a burst with power law exponents $\gamma = \gamma_1\gamma_2 \approx 1.45$ in Fig. 6(d) and $\gamma = \gamma_1\gamma_2 \approx 1.72$ in Fig. 7(d) within the main power law regimes. One expects that this power law will end in an exponential tail, which corresponds to interburst distances associated with large-amplitude relocations of sensor between the minima of $U(\phi)$. Indeed, the tail is single exponential in Fig. 7(d), with weight $c_c \approx 0.057$ and $\tau_c \approx 73.48$, which roughly corresponds to $\langle\tau_c\rangle \approx 79.43$ in Fig. 7(c). A corresponding single-exponential fit in Fig. 6(d) is, however, not that good, and a Pareto law fit at the same weight $c_p = c_c \approx 0.079$ and $\gamma = \gamma_1\gamma_2 \approx 1.42$ is visually better. This happened clearly by chance in a very particular case. Indeed, by choosing different thresholds in Figs. 6(a) and 6(b) one can see that there generally exists an exponential tail with a time constant which roughly corresponds to $\langle\tau_c\rangle$ in Fig. 6(c). This latter one is nicely described by the inverse Kramers rate. The weight c_c depends strongly on the choice of thresholds. The open times are nearly exponentially distributed in all parts of Figs. 6 and 7, with the time constants which depend strongly on the threshold choice. Important is that even if the mean residence times and the detailed structure of survival probabilities do strongly depend on the choice of thresholds, the time averaged portion of open time $p = \langle\tau_o\rangle/(\langle\tau_c\rangle + \langle\tau_o\rangle)$ is not changed dramatically. Its value approximately corresponds to the ensemble average depicted in Fig. 3 at $\psi = \pi$. This implies not only ergodicity, but also that a two-state reduction of continuous state dynamics is a reasonable one. With $\tau_{sc} \approx 0.404$ ms and $\tau_{sc} \approx 0.905$ ms estimated for the rods consisting of $n = 5$ and $n = 7$ magnetosomes, correspondingly (see in Appendix B) one has $\langle\tau_c\rangle \approx 7.15$ ms and $\langle\tau_o\rangle \approx 9.62$ ms in Fig. 6(d), as well as $\langle\tau_c\rangle \approx 4.16$ ms and $\langle\tau_o\rangle \approx 30.34$ ms in Fig. 7(d). These are typical time scales for ion channel gating dynamics. However, with the bursts neglected, the characteristic times lie in the hundreds of milliseconds range, which defines a characteristic time scale of the reaction of such a detector on changes of external magnetic field.

Furthermore, even in the absence of memory effects our model can explain the origin of power law distributions of closed times, $\psi_c(\tau) \propto \tau^{-\delta}$, with $\delta = 1 + \gamma$ in some range around $\delta = 2.5$, as our numerical results imply. Similar bursting fluctuations with $\delta \approx 2.24$ and exponentially distributed open times were indeed found in the locust large conductance BK channels [40]. A proper generalization for BK channels is, however, out of the scope of this work. It is reserved for the future. In this respect, one should mention that a very different phenomenological model was suggested earlier to rationalize bistable dynamics of BK channels in terms of a fractional conformational dynamics [46].

Our sensor operates, however, in viscoelastic cytosol, and a common line of reasoning is to account for the enlarged effective cytosol viscosity by using η_{eff} instead of η_0 within a Markovian Langevin dynamics [12]. This would mean the enlargement of τ_{sc} and the corresponding $\langle\tau_c\rangle$ and $\langle\tau_o\rangle$ by about the same factor. Then, already for $\eta_{\text{eff}} = 100\eta_0$ [12] the mean opening and closing times would become so large that such a magnetosensitive channel could not be of any potential relevance as a biosensor. It would be far too slow. However, our results obtained by a proper treatment of non-Markovian memory effects show that such simplistic estimations can be very misleading. Our model channel can yet be functional in a viscoelastic environment. It must be stressed that η_{eff} can only be finite if subdiffusion is transient and normal diffusion is established again for $t \gg \tau_h$. The central role is played, in fact, by the fractional friction coefficient $\eta_\alpha \sim \eta_{\text{eff}}\tau_h^{\alpha-1}$ and not by η_{eff}. Given the same η_α, $\eta_{\text{eff}} \sim \tau_h^{1-\alpha}$. By comparison of the results in Fig. 9(a) with the corresponding Markovian case depicted in Fig. 6(d) one establishes that the mean open and closed times are changed a little, for $\eta_{\text{eff}} = 100\eta_0$ and $\tau_h = 4.04$ s ($n = 5$), or $\tau_h = 9.05$ s ($n = 7$). Also, the initial Pareto law regime for the closed times is almost not affected in Fig. 9(a). This is because non-Markovian memory effects are still not at play on the relevant time scale smaller than τ_{in} of free subdiffusion. Diffusion is normal on that time scale. The latter feature is, however, not universally valid (see below) because (i) $\tau_{\text{in}} \sim \tau_h(\eta_0/\eta_{\text{eff}})^{1/(1-\alpha)}$ is strongly influenced by η_{eff} at fixed τ_h and (ii) the transition from initially normal dynamics to subdiffusional is also strongly affected by the presence of potential. Furthermore, the tails of distributions are changed dramatically. They became a stretched exponential, in agreement with [47,48], as a major

manifestation of viscoelastic effects. The stretched exponential tail of the closed time distribution describes the distribution of interburst time intervals, as can be understood from Fig. 8(a), where the bursts are neglected. The distribution of both open and closed times is almost stretched exponential in Fig. 8(a), except for an initial stage (see the inset in this figure). The mean residence times are somewhat enhanced with respect to the Markovian case in Fig. 6(a), in a good agreement with NMRT. The other choices of thresholds in Figs. 1(a) and 2(a) of the Supplemental Material [107] confirm these main features. Moreover, for a larger μB in Fig. 10(a) one observes similar features by comparison with Fig. 7(d): The mean residence times are about the same (within typical numerical error margins), and the exponential tails turn into the stretched exponential ones. However, the initial Pareto distribution in this cases is changed.

The observed features provide a general physical explanation for the emergence of stretched exponential distributions in the statistics of ion channel fluctuations, as observed first by Liebovitch *et al.* [35]. Our theory explains it as a manifestation of viscoelastic memory effects for the sensor dynamics in cytosol. This explanation is rather general. It is expected to hold also for other models of ion channel gating dynamics with the sensor moving within the membrane, or within the membrane protein itself. One should stress that the discussed results for fixed values of $\eta_{\rm eff}$ and τ_h are not expected to visibly change if we enlarge τ_h and $\eta_{\rm eff}$ so that η_α is not changed. This is because the main features we discuss are observed for the time intervals less than τ_h in our figures. A typical length of single stochastic trajectories used to obtain these figures exceeds greatly τ_h, and the diffusion becomes again normal on that time scale. What does matter indeed is the anomaly of diffusion caused by the memory of viscoelastic medium on the relevant time scales of transitions. For example, if we enhance τ_h by a factor of 100 (using two additional auxiliary Brownian particles in our simulations) and enhance $\eta_{\rm eff}$ by the factor of $100^{1-\alpha} \approx 15.9$ (for the used $\alpha = 0.4$), η_α is not changed, and we do not expect any significant changes of the results discussed. However, if we increase $\eta_{\rm eff}$ by the factor of ten at the same τ_h, η_α is tenfold increased, and this results into the further qualitative changes observed. What does matter indeed even for a finite τ_h is the fractional friction coefficient η_α.

Indeed, for $\eta_{\rm eff} = 1000$ with the same τ_h, the qualitatively new additional features are observed in the panel (b) of Figs. 9 and 10; see also Figs. 1(b) and 2(b) of Supplemental Material [107]. First, an initial power law emerges in the open time distribution, and a novel intermediate power law emerges in the closed time distribution. The mean residence times are essentially increased for the case with detection thresholds placed at $U(\phi)$ minima; see Figs. 8(b) and 11(b). However, in Figs. 9(b) and 11(b) they are a little increased (less than doubled). Hence, the gating dynamics of our model channel remains in a physiologically acceptable range. Such a sensor would slowly operate, yet be suitable to detect quasistatic or slowly changing magnetic fields. We see also how intermediate power law distributions can emerge naturally due to viscoelastic memory effects. Clearly, our theoretical approach is not restricted by a particular model of magnetosensitive ion channels we proposed and studied in this work.

V. CONCLUSIONS

In this paper we proposed and studied a model of magnetosensitive ion channels featured by a bistable magnetosensor moving in viscoelastic cytosol. It is shown that a cluster of ionic channels gated by such a sensor can operate for realistic parameters and provide a tentative explanation for biological manifestations of the influence of weak magnetic fields, in particular, such as navigation of different biological species in the magnetic field of Earth, as suggested earlier by Kirschvink *et al.* Our model provides also a natural explanation of the origin of stretched exponential and power law distributions in the statistics of ion current fluctuations as ones caused by the viscoelasticity of the medium in which the sensor operates. We believe that our study will spark a further interest, both theoretical and experimental, in the hypothesis of magnetosensitive ion channels and in the physical modeling of anomalous dynamics of ion channels and other proteins in living cells.

ACKNOWLEDGMENTS

Support of this research by the Deutsche Forschungsgemeinschaft (German Research Foundation), Grant No. GO 2052/1-2, is gratefully acknowledged.

APPENDIX A: ESTIMATION OF MAGNETIC MOMENTS AND MAGNETIC FIELD STRENGTHS

Consider a sphere of magnetite with radius R and saturation magnetization $M_s = 4.8 \times 10^5$ A/m. Assuming that it is magnetically ordered makes it possible to calculate its magnetic moment as $\mu = (4/3)\pi R^3 M_s$, which for a sphere of radius $R = 100$ nm yields $\mu \approx 2.01 \times 10^{-15}$ A m^2. The energy of such a sphere in the magnetic field of Earth estimated as $B_e = 50\ \mu$T is $E_M = \mu B_e \approx 10^{-19}$ J $\approx 24.5\ k_B T_r$, with $k_B T_r = 4.1 \times 10^{-21}$ J $= 4.1$ pN nm. The magnetic field produced by such a magnetic nanoparticle at the distances $r = |\vec{r}| \geqslant R$ from its center is the same as one of the point magnetic dipole μ located at its center [109],

$$\vec{B}(\vec{r}) = \frac{\mu_0}{4\pi}\left[\frac{3\vec{r}(\vec{\mu}\vec{r})}{r^5} - \frac{\vec{\mu}}{r^3}\right], \tag{A1}$$

where $\mu_0 = 4\pi \times 10^{-7}$ T m/A is magnetic permittivity of vacuum. This field is highly anisotropic and its maximal value near the surface of particle is

$$B_{\rm max} = \frac{\mu_0}{2\pi}\frac{\mu}{R^3} = \frac{2}{3}\mu_0 M_s \approx 0.402\ \text{T}. \tag{A2}$$

This is a very large field as compared with B_e. Notice that it does not depend on the particle radius and scales as $B_{\rm max}(R/r)^3$ with the distance $r \geqslant R$ from its center. Hence, up to the distances of about $r = 20R$ the maximum of the field produced by such a magnetic nanoparticle is larger than external B_e. For $R = 100$ nm, the corresponding distance is about 2 μm, a typical size of the bacterial cell. Given large E_M, such a particle is easily reoriented in the magnetic field of Earth. Together with a large $B_{\rm max}$ this provides a ground for the assertions that even quantum mechanisms can be mediated by the endogenous magnetic field of a magnetosome, rather than directly caused by the external magnetic field of Earth. Also,

the spatial gradient of such an endogenous magnetic field is large on nanoscale.

Furthermore, the magnetic energy of dipole-dipole interaction of two identical nanospheres separated by distance $r \geqslant 2R$ is

$$E_{dd} = V_{dd}(\sin\varphi_1 \sin\varphi_2 - 2\cos\varphi_1 \cos\varphi_2) \tag{A3}$$

in the approximation of point dipoles. Here one assumes for simplicity that the magnetic moments lie in a common plane making angles φ_1 and φ_2 with the line connecting their centers. Furthermore,

$$V_{dd} = 10^{-7}\frac{16}{9}\pi^2 M_s^2 R^3 \left(\frac{R}{r}\right)^3, \tag{A4}$$

which for the spheres in close contact, $r = 2R$, is

$$V_{dd} = 10^{-7}\frac{2}{9}\pi^2 M_s^2 R^3. \tag{A5}$$

For $R = 100$ nm, this yields $V_{dd} \approx 5.05 \times 10^{-17}$ J $\approx 1.23 \times 10^4\, k_B T_r$. This is a huge amount of energy. Even for $R = 10$ nm, $V_{dd} \approx 12.3\, k_B T_r$ is still large. This explains why such magnetic nanoparticles tend to make magnetically ordered chains at ambient temperatures, which are clearly seen in magnetotactic bacteria.

Several further remarks are required. First, $R = 100$ nm is about the maximal size of a spherical particle made of magnetite which possesses a permanent magnetic moment at ambient temperatures [10,11]. Larger spherical particles do not possess a permanent magnetic moment. They are in a multidomain superparamagnetic state. However, if the particle is elongated it can still be in a ferrimagnetic state at ambient temperatures. Next, the preferable direction of the magnetic moment is not completely fixed by the magnetic anisotropy of a Fe_3O_4 crystal and the form of a particle. When thermally agitated it can flip its direction to the opposite one; i.e., small nanoparticles are, in fact, intrinsically bistable. The corresponding thermal magnetic reorientation time (Neel relaxation time) exponentially depends on the particle volume. So, for $R = 11.5$ nm it is about 0.1 s only. However, already for $R = 15$ nm it is as large as 10^9 s ([92], p. 125), or about 32 yr; i.e., a metastable state can be considered as physically stable from a practical point of view. Furthermore, the physical anisotropy of a nanoparticle, e.g., an elongated ellipsoidal form, or the form of a rectangular parallelepiped further stabilizes the single domain structure. Many biomagnetite particles have proper sizes to be in the ferrimagnetic state. Typical sizes considered in this paper ensure the ferrimagnetic state at room and physiological temperatures. Notice also that the dipole-dipole interaction can also dramatically stabilize ferromagnetic order for small particles like $R = 10$ nm assembled into a chain.

APPENDIX B: ESTIMATION OF CHARACTERISTIC PHYSICAL TIME SCALE OF DYNAMICS

Here we estimate the rotational friction coefficient of a rod of length L and diameter d in fluid of viscosity ζ_0 following [110]. For this we use the rotational "end-over-end" diffusion coefficient D_0 [110] and the Einstein relation $\eta_0 = D_0/(k_B T)$. As a result,

$$\eta_0 = \frac{\pi \zeta_0 L^3}{3[\ln p + C]}, \tag{B1}$$

where $p = L/d$ is the aspect ratio and

$$C = -0.662 + 0.917/p - 0.050/p^2\ , \tag{B2}$$

which is valid for $p = 2$–20. For a magnetosome of size $a \times b \times b$ and the rod of length $L = na$, we approximate $d \approx b$, and $p \approx na/b$. Hence,

$$\eta_0 \approx n^3 \frac{\pi \zeta_0 a^3}{3[\ln(na/b) + C]} \tag{B3}$$

and

$$\tau_{sc} \approx n^3 \frac{\zeta_0 a^3}{U_0} \frac{\pi}{3[\ln(na/b) + C]}. \tag{B4}$$

In water, $\zeta_0 \sim 1$ mPa s at $T = 20\,^{\circ}$C, and for $U_0 = 41$ pN nm, $a = 55$ nm, we obtain $\zeta_0 a^3/U_0 \approx 4.058\ \mu$s. This yields for $b = 44$ nm and $n = 5$, $\tau_{sc} \approx 0.404$ ms and for $n = 7$, $\tau_{sc} \approx 0.905$ ms.

[1] S. J. Webb and D. D. Dodds, Nature (London) **218**, 374 (1968).
[2] N. D. Devyatkov, Sov. Phys. Usp. **16**, 568 (1974).
[3] W. Grundler and F. Keilmann, Phys. Rev. Lett. **51**, 1214 (1983).
[4] C. B. Grissom, Chem. Rev. **95**, 3 (1995).
[5] V. N. Binhi, *Magnetobiology: Underlying Physical Problems* (Academic Press, San Diego, CA, 2002).
[6] V. N. Binhi and A. V. Savin, Phys. Usp. **46**, 259 (2003).
[7] N. D. Devyatkov, M. B. Golant, and O. V. Betsky, *Millimeter Waves and Their Role in Vital Processes* (Radio and Svyaz, Moscow, 1991) [in Russian].
[8] F. S. Barnes and B. Greenebaum (eds.), *Handbook of Biological Effects of Electromagnetic Fields: Bioengineering and Biophysical Aspects of Electromagnetic Fields*, 3d ed. (Taylor & Francis, Boca Raton, FL, 2006).
[9] V. Pikov, X. Arakaki, M. Harrington, S. F. Fraser, and P. H. Siegel, J. Neural Eng. **7**, 045003 (2010).
[10] J. L. Kirschvink, D. S. Jones, and B. J. MacFadden (eds.), *Magnetite Biomineralization and Magnetoreception in Organisms: A New Biomagnetism* (Plenum Press, New York, 1985).
[11] J. L. Kirschvink and J. L. Gould, Biosystems **13**, 181 (1981).
[12] J. L. Kirschvink, Phys. Rev. A **46**, 2178 (1992).
[13] W. Wiltschko and R. Wiltschko, J. Comp. Physiol. A **191**, 675 (2005).
[14] K. Schulten, C. E. Swenberg, and A. Weller, Z. Phys. Chem. **111**, 1 (1978); T. Ritz, S. Adem, and K. Schulten, Biophys. J. **78**, 707 (2000); C. T. Rodgers and P. J. Hore, Proc. Natl. Acad. Sci. USA **106**, 353 (2009).
[15] R. K. Adair, Phys. Rev. A **43**, 1039 (1991); Proc. Natl. Acad. Sci. USA **91**, 2925 (1994).
[16] R. Blakemore, Science **190**, 377 (1975).
[17] D. Faivre and D. Schüler, Chem. Rev. **108**, 4875 (2008).

[18] B. Devouard, M. Posfai, X. Hua, D. Bazylinski, R. B. Frankel, and P. R. Buseck, Am. Mineral. **83**, 1387 (1998).

[19] L. G. Abracado, F. Abreu, C. N. Keim, A. P. C. Campos, U. Lins, and M. Farina, Phys. Biol. **7**, 046016 (2010).

[20] J. L. Kirschvink, A. Kobayashi-Kirschvink, and B. J. Woodford, Proc. Natl. Acad. Sci. USA **89**, 7683 (1992).

[21] S. H. K. Eder, H. Cadiou, A. Muhamad, P. A. McNaughton, J. L. Kirschvink, and M. Winklhofer, Proc. Natl. Acad. Sci. USA **109**, 12022 (2012).

[22] N. B. Edelman *et al.*, Proc. Natl. Acad. Sci. USA **112**, 262 (2015).

[23] J. Dobson, Exp. Brain Res. **144**, 122 (2002).

[24] V. N. Binhi and D. S. Chernavskii, Europhys. Lett. **70**, 850 (2005); V. N. Binhi, Bioelectromagnetics **27**, 58 (2006); Int. J. Radiat. Biol. **84**, 569 (2008).

[25] J. Vanderstaeten and P. Gillis, Bioelectromagnetics **31**, 371 (2010).

[26] V. P. Shcherbakov, M. Winklhofer, M. Hanzlik, and N. Petersen, Eur. Biophys. J. **26**, 319 (1997).

[27] A. Körnig, J. Dong, M. Bennet, M. Widdrat, J. Andert, F. D. Müller, D. Schüler, S. Klumpp, and D. Faivre, Nano Lett. **14**, 4653 (2014).

[28] E. D. Yorke, J. Theor. Biol. **77**, 101 (1979).

[29] M. Winklhofer and J. L. Kirschvink, J. R. Soc. Interface **7**, S273 (2010).

[30] L. Yan and S. Tao, Chin. Phys. B **22**, 048701 (2013).

[31] D. Mohanta, E. Stava, M. Yu, and R. H. Blick, Phys. Rev. E **89**, 012707 (2014).

[32] S. M. Bezrukov, R. P. Rand, I. Vodyanoy, and V. A. Parsegian, Faraday Discuss. **111**, 173 (1998).

[33] M. B. Jackson, *Molecular and Cellular Biophysics* (Cambridge University Press, Cambridge, UK, 2006).

[34] J. Howard and A. J. Hudspeth, Neuron **1**, 189 (1988); A. J. Hudspeth, Y. Choe, A. D. Mehta, and P. Martin, Proc. Natl. Acad. Sci. USA **97**, 11765 (2000).

[35] L. S. Liebovitch and J. M. Sullivan, Biophys. J. **52**, 979 (1987).

[36] T. L. Croxton, Biochim. Biophys. Acta **946**, 19 (1988).

[37] P. Läuger, Biophys. J. **53**, 877 (1988).

[38] G. L. Millhauser, E. E. Salpeter, and R. E. Oswald, Proc. Natl. Acad. Sci. USA **85**, 1503 (1988).

[39] M. S. P. Sansom, F. G. Ball, C. J. Kerry, R. McGee, R. L. Ramsey, and P. N. R. Usherwood, Biophys. J. **56**, 1229 (1989).

[40] E. Gorczynska, P. L. Huddie, B. A. Miller, I. R. Mellor, H. Vais, R. K. Ramsey, and P. N. R. Usherwood, Pfluegers Arch. **432**, 597 (1996); S. Mercik and K. Weron, Phys. Rev. E **63**, 051910 (2001).

[41] Z. Qu, G. Hu, A. Garfinkel, and J. N. Weiss, Phys. Rep. **543**, 61 (2014).

[42] R. H. Austin, K. Beeson, L. Eisenstein, H. Frauenfelder, I. C. Gunsalus, and V. P. Marshall, Phys. Rev. Lett. **32**, 403 (1974).

[43] H. Frauenfelder, S. G. Sligar, and P. G. Wolynes, Science **254**, 1598 (1991); H. Frauenfelder, P. W. Fenimore, G. Chen, and B. H. McMahon, Proc. Natl. Acad. Sci. USA **103**, 15469 (2006); H. Frauenfelder *et al.*, *ibid.* **106**, 5129 (2006).

[44] S. M. Rappaport, O. Teijido, D. P. Hoogerheide, T. K. Rostovtseva, A. M. Berezhkovskii, and S. M. Bezrukov, Eur. Biophys. J. **44**, 465 (2015).

[45] I. Goychuk and P. Hänggi, Proc. Natl. Acad. Sci. USA **99**, 3552 (2002); Physica A (Amsterdam, Neth.) **325**, 9 (2003).

[46] I. Goychuk and P. Hänggi, Phys. Rev. E **70**, 051915 (2004).

[47] I. Goychuk, Phys. Rev. E **80**, 046125 (2009).

[48] I. Goychuk, in *Advances in Chemical Physics*, edited by S. A. Rice and A. R. Dinner (John Wiley & Sons, Hoboken, NJ, 2012), Vol. 150, pp. 187–253.

[49] J.-H. Jeon, Hector Martinez-Seara Monne, M. Javanainen, and R. Metzler, Phys. Rev. Lett. **109**, 188103 (2012).

[50] T. G. Mason and D. A. Weitz, Phys. Rev. Lett. **74**, 1250 (1995).

[51] F. Amblard, A. C. Maggs, B. Yurke, A. N. Pargellis, and S. Leibler, Phys. Rev. Lett. **77**, 4470 (1996).

[52] A. Caspi, R. Granek, and M. Elbaum, Phys. Rev. E **66**, 011916 (2002).

[53] D. Mizuno, C. Tardin, C. F. Schmidt, and F. C. MacKintosh, Science **315**, 370 (2007).

[54] T. A. Waigh, Rep. Prog. Phys. **68**, 685 (2005).

[55] J. Szymanski and M. Weiss, Phys. Rev. Lett. **103**, 038102 (2009).

[56] I. Santamaria-Holek, J. M. Rubi, and A. Gadomski, J. Phys. Chem. B **111**, 2293 (2007).

[57] G. Guigas, C. Kalla, and M. Weiss, Biophys. J. **93**, 316 (2007); M. Weiss, Phys. Rev. E **88**, 010101 (2013).

[58] S. C. Weber, A. J. Spakowitz, and J. A. Theriot, Phys. Rev. Lett. **104**, 238102 (2010).

[59] C. Wilhelm, Phys. Rev. Lett. **101**, 028101 (2008); D. Robert, Th.-H. Nguyen, F. Gallet, and C. Wilhelm, PLoS One **4**, e10046 (2010).

[60] L. Bruno, M. Salierno, D. E. Wetzler, M. A. Desposito, and V. Levi, PLoS One **6**, e18332 (2011).

[61] S. C. Kou and X. S. Xie, Phys. Rev. Lett. **93**, 180603 (2004).

[62] S. A. Adelman, J. Chem. Phys. **64**, 124 (1976); P. Hänggi and H. Thomas, Z. Phys. B **26**, 85 (1977); P. Hänggi, H. Thomas, H. Grabert, and P. Talkner, J. Stat. Phys. **18**, 155 (1978); P. Hänggi, Z. Phys. B **31**, 407 (1978).

[63] I. Goychuk and P. Hänggi, Phys. Rev. Lett. **99**, 200601 (2007).

[64] P. Siegle, I. Goychuk, P. Talkner, and P. Hänggi, Phys. Rev. E **81**, 011136 (2010); P. Siegle, I. Goychuk, and P. Hänggi, Phys. Rev. Lett. **105**, 100602 (2010); Europhys. Lett. **93**, 20002 (2011).

[65] I. Goychuk and P. Hänggi, in *Fractional Dynamics: Recent Advances*, edited by J. Klafter, S. C. Lim, and R. Metzler (World Scientific, Singapore, 2011), Chap. 13, pp. 307–329.

[66] I. Goychuk, Chem. Phys. **375**, 450 (2010).

[67] I. Goychuk and V. Kharchenko, Phys. Rev. E **85**, 051131 (2012).

[68] I. Goychuk and V. Kharchenko, Math. Model. Nat. Phenom. **8**, 144 (2013).

[69] V. O. Kharchenko and I. Goychuk, Phys. Rev. E **87**, 052119 (2013).

[70] V. Kharchenko and I. Goychuk, New J. Phys. **14**, 043042 (2012).

[71] I. Goychuk, V. O. Kharchenko, and R. Metzler, PLoS One **9**, e91700 (2014).

[72] I. Goychuk, V. O. Kharchenko, and R. Metzler, Phys. Chem. Chem. Phys. **16**, 16524 (2014).

[73] I. Goychuk, Phys. Biol. **12**, 016013 (2015).

[74] K. Luby-Phelps, Mol. Biol. Cell **24**, 2593 (2013).

[75] I. Goychuk, Phys. Rev. E **86**, 021113 (2012).

[76] T. Odijk, Biophys. J. **79**, 2314 (2000); L. Masaro and X. X. Zhu, Prog. Polym. Sci. **24**, 731 (1999); R. Holyst *et al.*, Phys. Chem. Chem. Phys. **11**, 9025 (2009).

[77] B. R. Parry, I. V. Surovtsev, M. T. Cabeen, C. S. O'Hern, E. R. Dufresne, and C. Jacobs-Wagner, Cell **156**, 183 (2014).
[78] H. A. Kramers, Physica (Amsterdam) **7**, 284 (1940).
[79] R. F. Grote and J. T. Hynes, J. Chem. Phys. **73**, 2715 (1980).
[80] P. Hänggi and F. Mojtabai, Phys. Rev. A **26**, 1168 (1982).
[81] B. Carmeli and A. Nitzan, J. Chem. Phys. **79**, 393 (1983).
[82] E. Pollak, H. Grabert, and P. Hänggi, J. Chem. Phys. **91**, 4073 (1989).
[83] P. Hänggi, P. Talkner, and B. Borkovec, Rev. Mod. Phys. **62**, 251 (1990).
[84] I. Goychuk, Fluct. Noise Lett. **11**, 1240009 (2012).
[85] I. Goychuk and V. O. Kharchenko, Phys. Rev. Lett. **113**, 100601 (2014).
[86] M. Herrchen and H. C. Öttinger, J. Non-Newtonian Fluid Mech. **68**, 17 (1997).
[87] H. Kojima, E. Muto, H. Higuchi, and T. Yanagida, Biophys. J. **73**, 2012 (1996).
[88] Ch. Koch, *Biophysics of Computation: Information Processing in Single Neurons* (Oxford University Press, New York, 1999).
[89] R. Kubo, Rep. Prog. Phys. **29**, 255 (1966); R. Kubo, M. Toda, and M. Hashitsume, *Nonequilibrium Statistical Mechanics*, 2nd ed. (Springer, Berlin, 1991).
[90] G. W. Ford, M. Kac, and P. Mazur, J. Math. Phys. **6**, 504 (1965); G. W. Ford, J. T. Lewis, and R. F. O'Connell, Phys. Rev. A **37**, 4419 (1988).
[91] R. Zwanzig, *Nonequilibrium Statistical Mechanics* (Oxford University Press, Oxford, UK, 2001).
[92] W. T. Coffey and Y. P. Kalmykov, *The Langevin Equation, With Applications to Stochastic Problems in Physics, Chemistry and Electrical Engineering*, 3d ed. (World Scientific, New Jersey, 2012).
[93] A. Gemant, Physics **7**, 311 (1936).
[94] W. B. Russel, D. A. Saville, and W. R. Schowalter, *Colloidal Dispersions* (Cambridge University Press, Cambridge, UK, 1989).
[95] R. Metzler and J. Klafter, Phys. Rep. **339**, 1 (2000).
[96] F. Mainardi and P. Pironi, Extr. Math. **11**, 140 (1996); arXiv:0806.1010 (2008).
[97] E. Lutz, Phys. Rev. E **64**, 051106 (2001).
[98] U. Weiss, *Quantum Dissipative Systems*, 2nd ed. (World Scientific, Singapore, 1999).
[99] I. Goychuk, Phys. Rev. E **76**, 040102(R) (2007).
[100] J. H. P. Schulz, E. Barkai, and R. Metzler, Phys. Rev. X **4**, 011028 (2014).
[101] I. Goychuk, Commun. Theor. Phys. **62**, 497 (2014).
[102] H. Stehfest, Commun. ACM **13**, 47 (1970); **13**, 624 (1970)(Erratum).
[103] I. Goychuk and P. Hänggi, Chem. Phys. **324**, 160 (2006).
[104] J. N. Israelachvili, *Intermolecular and Surface Forces*, 3d ed. (Academic Press, Waltham, MA, 2011).
[105] T. D. Pollard, W. C. Earnshow, and J. Lippincott-Schwartz, *Cell Biology*, 2nd ed. (Saunders Elsevier, Philadelphia, 2007).
[106] B. C. Arnold, *Pareto Distributions*, 2nd ed. (CRC Press, Boca Raton, FL, 2015).
[107] See Supplemental Material at http://link.aps.org/supplemental/10.1103/PhysRevE.92.042711 for additional analysis.
[108] The choice $p_1 = p_2$ is not appropriate because, given an ideal time resolution of current recordings, one would detect many false open-shut transitions corresponding to erratic fluctuations (fast recrossings) around the threshold value $\phi_{\rm th}$ solving $p_1(\phi_{\rm th}) = p_2(\phi_{\rm th}) = 0.5$. Such fast recrossings simply do not correspond to transitions between two macrostate.
[109] J. D. Jackson, *Classical Electrodynamics*, 3d ed. (Wiley, New York, 1999).
[110] J. Garcia de la Torre and V. Bloomfield, Q. Rev. Biophys. **14**, 81 (1981).